Three-dimensional Characterization of the Wake Flow behind Different Vortex Generators

by

Sen Wang

A thesis submitted in partial fulfillment of the requirements for the degree of

Master of Science

Department of Mechanical Engineering
University of Alberta

Abstract

Vortex generators (VGs) are widely applied passive flow control devices that are proven to have significant effect in enhancing the performance of an aerodynamic system. With the recent development in non-intrusive measurement techniques, and computing ability, it has become possible to measure and simulate three-dimensional flow fields behind VGs. The objective of this investigation was to determine the effect that the shape of VGs may have on the wake flow through measuring the turbulence statistics and three-dimensional coherent structures.

The experiment examined seven VGs including non-conventional and vane-type VGs. Non-conventional VGs referred to wishbone, doublet and ramp which have wedge-element. Vane-type VGs had rectangular, trapezoidal, and delta vane-blades. VGs were installed in a thin laminar boundary layer at Reynolds number of 930, based on the VG height and freestream velocity. For non-conventional VGs, planar particle image velocimetry (PIV) and stereoscopic PIV (stereo-PIV) measurements were conducted to measure the mean flow and turbulence statistics with high spatial-resolution. For both non-conventional VGs and vane-type VGs, time-resolved tomographic PIV (tomo-PIV) measurement was also carried out in a $92 \times 55 \times 13$ mm^3 volume at 800 Hz frequency to visualize the vortical structures and their evolution.

The analysis of the non-conventional VGs consisted of characterizing the mean wake flow, determining the coherent structures and visualizing their evolution. The result suggests that the wishbone VG has the best performance in enhancing flow mixing. The wishbone VG also shows the fastest velocity recovery, followed by the doublet VG and the ramp VG. The peak of turbulence production in the wake of the wishbone and doublet VG has a similar magnitude, and is stronger than the peak in the wake of the ramp VG. The ramp VG produces the most coherent

vortical structures based on the three-dimensional visualization. The perturbations caused by the second wedge of the doublet VG breaks down the primary vortex and transfer the energy to smaller structures. Although all the VGs being examined in this study have V-shape geometry, the wishbone VG with the least VG wetted area has the best performance in terms of mixing, while the doublet VG produced the highest level of turbulence.

The investigation of the vane-type VGs focused on evaluating the device drag, comparing the three-dimensional mean flow field, and visualizing the instantaneous coherent structures. The momentum deficit analysis illustrated that rectangular vane VG produced the largest parasitic drag, followed by the trapezoidal vane VG and delta vane VG. The single rectangular vane VG presented a device drag larger than the trapezoidal vane VG and smaller than the rectangular vane VG. The measurements showed that the rectangular VG produced the strongest streamwise vortices and has the highest level of mean vorticity fluctuation and turbulence production. The instantaneous visualizations showed that the dominant primary vortex was a pair of counter-rotating streamwise vortices. The secondary vortices were observed to be wall-normal vortices. The investigation of the instantaneous coherent structure indicated that the coherency and strength of the generated vortex structure is inversely proportional to the sweep angle of the vane leading-edge. The analysis showed that the effective wall-normal mixing distance is a significant factor in selecting VG, regarding the device drag and flow control effectiveness.

Preface

This thesis includes the experimental measurement and analysis about the wakes of seven vortex generators, carried out by me under supervision of Dr. Sina Ghaemi.

The experiments in this work were conducted by me under supervision of Dr. Sina Ghaemi, in the water flume located in Natural Resources Engineering Facility (NREF). The flat plate and the models of vortex generators were designed by me. The vortex generators were 3D printed in Dr. David Nobes laboratory

The processing of tomo-PIV data used the volume deformation iterative multi-grid technique (VODIM) developed by Prof. Fulvio Scarano.

The analysis and interpretation of the experimental result from Chapter 4 and Chapter 5 was conceived by me under supervision of Dr. Sina Ghaemi.

Table of Contents

List of Figures

List of Tables

Chapter 1.   Introduction

Flow separation poses a performance limit when designing aerodynamic systems, such as diffusers, turbines, and aerodynamic vehicles. Several active and passive flow control methods have been developed in the past several decades. A widely applied passive method is installing VG to delay or prevent separation by enhancing the wall-normal flow mixing (Taylor, 1947; Schubauer and Spangenberg, 1960; Lin, 2002). As a result, VGs have the potential to increase lift and the stall angle-of-attack of an airfoil, and reduce the drag caused by flow separation. Numerous designs of VGs, including vane-type VGs and non-conventional VGs (United States of America Patent No. 4455045, 1991a; United States of America Patent No. 5058837, 1991b) have been applied in the past. However, there are limited studies about the performance of VG from the perspective of the effect of three-dimensional design on vortex structures within the immediate wake. This has motivated the current study to investigate VGs with different shapes through comparing the turbulent characteristics and three-dimensional coherent structures.

The first VG was introduced in 1947 (Taylor, 1947), as a row of surface mounted metal vanes inclined with respect to flow. More VG designs were developed in the last several decades, including ramp, and wheeler type VGs (United States of America Patent No. 4455045, 1991a; United States of America Patent No. 5058837, 1991b). Most investigations only focused on characterizing the mean flow field using Laser Doppler Anemometry (LDA) (Lin, 1999; Betterton et al., 2000) and 2D PIV (Godard and Stanislas, 2006) before the three-dimensional PIV techniques become mature. The flow control effectiveness and vortex structures were mostly determined by comparing the separation line using visualization technique such as oil-flow (Schubauer and Spangenberg, 1960; Lin et al., 1990a), and smoke filament (Barrett and Farokhi, 1993). The dominant flow structure from the mean flow field was determined to be streamwise vortices (Godard and Stanislas, 2006; Lin, 1999; Betterton et al., 2000; Barrett and Farokhi, 1993). The vortices can be counter-rotating or co-rotating depend on the arrangement and geometry of the VGs.

The geometric parameters, such as VG height (Kuethe, 1972; Lin, 1999; Lin, 2002), inclination (Godard and Stanislas, 2006), and chord length (Lin, 1999; Froster and White, 2014) were

studied to improve the VG performance. Some investigations (Lin, 1999; Lin et al., 1991; Lin et al., 1990a; Lin et al., 1990b) evaluated the flow control effectiveness of VGs with different shapes. The non-conventional VGs, usually mechanically stronger than vane-type VG, can achieve similar flow control performance as the vane-type VG with a lower device drag. However, most analysis was still two-dimensional, and the visualization of the coherent structure was not clear due to the technique restrictions.

The numerical investigations of VG were able to provide more three-dimensional information about the wake flow compared to the traditional experimental methods. In the study conducted by Forster and White (2014), the flow field around a ramp VG on a heavily-cambered wing was simulated using Reynolds-averaged Navier-Stokes (RANS) turbulence model. The three-dimensional streamlines over the VGs were presented, and the change of the flow pattern in streamwise direction was illustrated over the entire wing. With the development in tomo-PIV, the instantaneous three-dimensional wake flow of VGs can be experimentally measured. The investigations of Sun et al. (2016) and Ye et al. (2016) captured the hairpin vortices and their evolution within the instantaneous wake of micro-ramp VGs. They also highlighted the importance of characterizing the coherent structures to identify the mechanism of mixing and separation control by different VGs.

The recent experimental investigations provided more detail about the wake of VG by three-dimensional measurement of the instantaneous wake flow. However, there is still lack of understanding about the effect of the VG shape. The purpose of this experiment is to investigate the turbulent characteristics and coherent structures in the wake of various vane-type VGs and non-conventional VGs. Planar particle image velocimetry and stereoscopic PIV (stereo-PIV) will be applied to characterize the velocity, the Reynolds stresses, and the vorticity fields with high spatial-resolution in several planes across the wake region of non-conventional VGs. The spatial organization of the generated vortical structures and the temporal evolution of the vortical structures will be investigated using tomo-PIV. The results identify the effect of VG shape on the mixing mechanism and the flow development.

The thesis outline is listed and explained as following:

Chapter 2: Background review about the current study is stated. The first section discusses flow separation. A brief description of flow separation is followed by its corresponding impact on aerodynamic systems. The background introduction of VG is provided. The measurement techniques used in this experiment are introduced, including planar, stereo, and tomo-PIV.

Chapter 3: The experimental setup including flow facility, examined VG models, and the measurement systems are introduced. The details of data processing are stated

Chapter 4: The turbulent characteristics and coherent structures in the wake of VGs are compared. The evaluation of non-conventional VGs is made based on planar, stereo, and high speed tomo-PIV measurement. The comparison of vane-type VGs are carried out using tomo-PIV measurement.

Chapter 5: The effect of shape of VGs on flow mixing mechanism, and vortex shedding are concluded.

Chapter 2. Literature review

2.1 Flow separation

The separation of the boundary layer from a surface can occur due to an adverse pressure gradient (APG) or a sharp geometric discontinuity. As described in previous literatures (Simpson, 1981; Sears and Telionis, 1975; Shen, 1979), flow separation is an entire process of the "departure", "breakaway", or the breakdown of the boundary layer flow. It is generally explained as a response at which the near wall region maintains interaction with the free stream flow (Simpson, 1981). This results in an abrupt thickening of the boundary layer followed by the lift-up of the flow from the surface by a large wall-normal velocity (Simpson, 1981). In terms of two-dimensional flow separation, a terminology was proposed at the Colloquium on Flow Separation (Simpson, 1979) to better describe the flow separation phenomenon: Detachment, reattachment, separation, stall, and stalled fluid. The definition of each term is given in Table 2.1.

Table 2.1. Terminology of flow separation (Simpson, 1979)

Terminology	Definition
Detachment	The location where the limiting streamline leaves the wall surface.
Reattachment	The location where the limiting streamline rejoins the wall surface.
Separation	The process of detachment, recirculation, or reattachment without free wake. In case of wake flow, a free-shear layer between the free stream and near still wake region is developed.
Stall	Pressure force created by recirculated flow zone.
Stalled fluid	Fluid that has zero velocity or moving in reversed direction within the recirculating zone.

The feature of flow separation within a steady, freestream, two-dimensional turbulent boundary layer was characterized through a series of laser anemometer measurements (Simpson et al., 1977; Simpson et al., 1981a; Simpson et al., 1981b; Shiloh et al., 1981). In the region upstream of the separation, it is acknowledged that the qualitative turbulence structure from a turbulent boundary layer in an APG has similar characteristics with respect to a zero-pressure gradient case (Simpson, 1981). The mean two-dimensional velocity profile can be described using the "law of the wall" and the "law of the wake" (Coles, 1956). Other important parameters such as the turbulence energy, dissipation, production, and spectral distributions also have known behavior (Simpson, 1981). Based on 145 mean velocity profiles from Coles and Hirst (1969),

Perry and Schofield (1973) proposed a mean velocity profile correlation for the unseparated flow under APG that has a maximum turbulent shear stress, $-\langle uv \rangle$, larger than 1.5 (τ_w /ρ). In the region near separation described by the above correlation, the normal stress terms $\partial(\langle u^2 \rangle - \langle v^2 \rangle)/\partial x$ and $(\langle u^2 \rangle - \langle v^2 \rangle)\partial U/\partial x$ had a significant value. As the separation point was approached, approximately one third of the turbulence production was due to the normal stress effect in the outer region (Simpson et al., 1977; Simpson et al., 1981b).

Three types of wing stalls caused by flow separation were listed: (1) the thick airfoil gentle stall, which the turbulent flow separation moves towards the leading edge, (2) the laminar flow separation at the leading edge without reattachment, and (3) the laminar flow separation with reattachment (Carmichael, 1981).

The performance of low-Reynolds number airfoils is highly affected by the poor separation behavior since the boundary layer may still be laminar and is not capable of resisting intense APG (Lissaman, 1983). When the Reynolds number based on chord length is below 30,000, the boundary layer can be completely laminar for small angle-of-attacks. However, as the APG increases, the laminar separation may occur and can cover the entire airfoil which extends into the wake (Lissaman, 1983). This separation extremely limits the lift generated by the airfoil, and significantly increases the drag force. In another case, the separated layer will transit into turbulent flow and reattach to the airfoil surface and form a laminar separation bubble. The distance between the departure point and reattachment point can be expressed as a bubble length-based Reynolds number (Lissaman, 1983). The separation to transition Reynolds number was found by von Doenhoff to be Re ≈ 50,000 (Carmichael, 1981). Hence, the possibility of having reattachment is low if the airfoil has a chord magnitude close to the bubble length. More generally, the separation to turbulent reattachment Reynolds number was observed to be 70,000 (Lissaman, 1983). The separation bubble had a length of about 20% to 30% of the airfoil chord at a Reynolds number around 10^5. The length will be shortened to few percent of the chord length as the Reynolds number further increases (Lissaman, 1983). Thus, the airfoil performance will not be significantly affected. As the angle of attack increases, the short separation bubble can burst into a long bubble due to the increase in required pressure recovery for reattachment. The long bubble, however, has severe disturbance to the airfoil performance by triggering stall (Lissaman, 1983).

2.2 Vortex generator

2.2.1 Separation control

VGs are surface mounted protrusions, which are widely applied as a passive flow control device to delay or prevent flow separation. As discussed by Schubauer and Spangenberg (1960), the flow will cease due to the buildup pressure at wall and lead to flow separation. The molecular diffusion cannot provide enough mixing to support the flow with momentum against the pressure rise. The stirring of the slow near wall flow and fast external flow appears to be necessary. The corresponding mixing occurs in turbulent flow, and the effect is known as the eddy viscosity ($<uv>$). It grants the turbulent flow great self-mixing ability, which allows it to deal with higher pressure rises than laminar flow. However, the upper limit of such self-mixing is still low, and a more efficient mixing was sought instead of natural mixing. The aim of the separation control devices is to remove the momentum deficient fluid by injecting tangential momentum laden flow, or energize low-speed near wall flow by passively inducting high speed flow towards the wall. Tangential injection approach is not favored since it contains flow ducting and energy requirement, which complicates the system. As a result, the latter approach is preferred by most manufacturers.

In 1947, boundary layer control using VG was first introduced by Bruynes and Taylor from the United Aircraft Corporation (Taylor, 1947). The investigation was performed on a row of plates and airfoils that project normal to the surface at a side-slip angle with respect to the free-stream to create streamwise trailing vortices. The height (h) of these VGs was on the order of the boundary layer thickness (δ). The high momentum flow is continuously swept towards the wall surface in helical paths and replaces the retarded flow to a certain extent. The boundary layer retardation and growth caused by the wall friction and APG is opposed by this re-energization process. Schubauer and Spangenberg (1960) investigated the effect of large VGs ($h \approx \delta$) with various shapes on development of a turbulent boundary layer under APG. They observed that all VGs reduced the APG by transferring high velocity flow to the near-wall region. This reduced the thickness of the boundary layer, relaxed the APGs, and provided the fluid with sufficient streamwise momentum to remain attached to the wall (Schubauer and Spangenberg, 1960). As a result, flow separation was prevented or postponed to a downstream location.

2.2.2 Types of vortex generator

Vane-type VGs are the most common VGs. They usually consist of a row of metal vanes, installed on the surface where flow separation occurs. First investigated by Taylor (1947), they have been widely applied for both civilian and military use in the past decades due to their simplicity and efficiency. Vane-type VGs can be distinguished by their vane-blade shape. Some typical examples are shown in Figure 2.1: (a) rectangular vane, (b) trapezoidal vane, and (c) delta vane.

<div align="center">(a)　　　　　　　　　(b)　　　　　　　　　(c)</div>
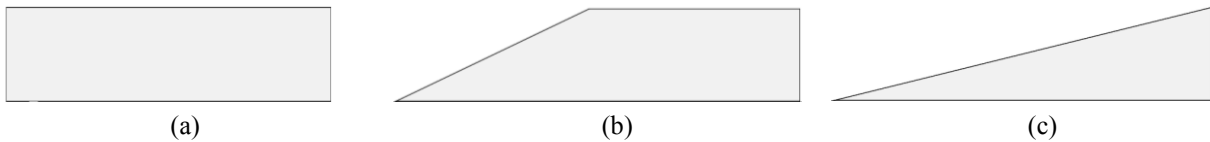
Figure 2.1. Typical vane-blade shape: (a) rectangular vane, and (b) trapezoidal vane and (c) delta vane.

VGs with wedge-element were introduced later with the objective to produce stronger streamwise vortices when compared to vane-type VGs. This effectively provides sufficient flow mixing at a lower device height (Lin, 1990). The most common non-conventional VGs are the doublet (United States of America Patent No. 4455045, 1991a), wishbone (United States of America Patent No. 5058837, 1991b), and ramp as shown in Figure 2.2. These VGs are mechanically stronger and easier to apply than the vane-type VGs (Lin, 1990).

<div align="center">(a)　　　　　　　　　(b)　　　　　　　　　(c)</div>
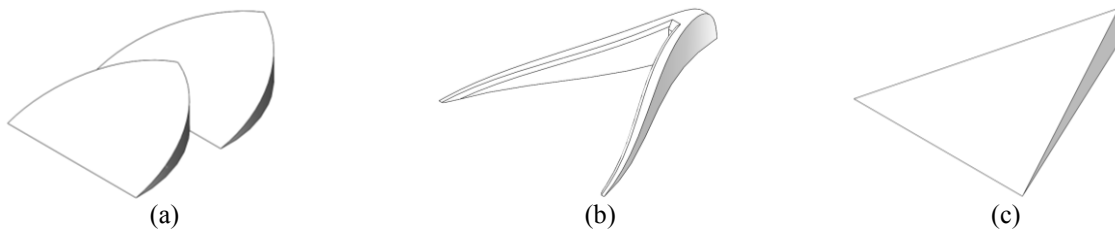
Figure 2.2. Three common seen non-conventional VGs: (a) doublet, and (b) wishbone and (c) ramp.

2.2.3 Vortex generator arrangement

Two adjacent vanes with opposite incidence angle β can be considered as one type of VG arrangement, which is capable of generating counter-rotating streamwise vortices (e.g. the left two vanes in Figure 2.3a). The wedge-element VGs, such as wishbone, doublet and ramp, can be treated as counter-rotating arranged vane-type VGs with no gap. The generated trailing vortices are effective in delaying the flow separation when they are in counter-rotating arrangement, and the boundary layer is also thin between alternate pairs of vortices (Pearcey, 1961). These

counter-rotating vanes and wedge-element VGs are referred as V-shape VGs in this study. In the investigation conducted by Pearcey (1961), this vortex arrangement, has a short effective life in streamwise direction, compared to the co-rotating vortices arrangement. The counter-rotating vortices tend to move closer as the streamwise distance increases, and generate an induced resultant velocity that moves away from the wall (Acalar and Smith, 1987). The vortices are eventually dampened out, and the boundary layer thickness is approximately doubled from $1.6h$ downstream to $12.8h$ (Pearcey, 1961). The effectiveness of counter-rotating VGs was also confirmed by Betterton et al. (2000) and Janiszewska et al. (2004). Lin (1999) demonstrated that delta and trapezoidal vanes arranged in V-shape are effective to generate counter-rotating vortices. Rao and Kariya (1988) investigated the effectiveness of low-profile VGs (height = 0.6δ) with vane-type and semi-circular geometries. They measured both static pressure and total pressure loss to evaluate the VGs ability to control an APG-induced separation over a flat plate. Their results showed that the performance of V-shape VGs was less sensitive to geometric parameters such as height, incidence angle, and chord length of the elements. It suggested that the V-shape VGs have higher geometry tolerance in practical applications.

The co-rotating system, shown in Figure 2.3b, has the VG vanes in a row with the same incidence angle β with respect to the flow direction. All the trailing streamwise vortices have the same rotation direction. For a co-rotating system, the most important factor on flow control effectiveness is the spacing between the vanes (Pearcey, 1961). If the spacing is too close, the low momentum fluid swept out by one streamwise vortex will be absorbed into the near wall region by the adjacent streamwise vortex; which damps the vortex. The most effective pattern is to have the spacing no less than $3h$ (Pearcey, 1961). Thus, the corresponding performance is comparable to the counter-rotating system. When the spacing is above $3h$, the effectiveness of a co-rotating system only falls slightly.

Figure 2.3. Vane-type VGs with (a) counter-rotating and (b) co-rotating arrangement.

2.2.4 Drag penalty

The early large VGs have been successfully applied on many aerodynamic applications for separation control purposes. Industrial applications suggest that these VGs generate residual drag in the wake regions. The parasitic drag consists of the following categories: the drag on the VG blade, the induced drag associated with the energy in the vortices, the interference drag from disturbing the pressure distribution, and the skin friction induced by the vortex action (Pearcey, 1961). The net drag will be the sum of the drag mentioned above and the amount of reduction in the form drag. As suggested by Pearcey (1961), the VG should be carefully selected to be as small as possible to generate minimum vortex strength for the required range of effectiveness. The flow control requirement and corresponding VG geometry parameters will vary from application to application. In practice, a procedure of optimizing the VG installation was described by Pearcey (1961): (1) generating more than adequate vortex strength per unit span and observing the excess in effectiveness, (2) experimentally reducing the number of VGs or the size of VGs to achieve an optimum compromise between the drag and separation point control. This procedure works particularly well for co-rotating VG arrangements since their vortex path is not sensitive to the spacing and vortex strength.

The drag penalty of large VGs can be reduced by deploying them only when flow separation is anticipated. For example, it is desirable to deploy VGs during landing or take-off of a flight when large lift is needed, and retract the VGs during the cruise phase to reduce drag. However, active deployment of the VGs can increase the complexity of the system. In that case, adjusting the size of VGs appears to be the favorable option.

2.2.5 Low-profile vortex generator

To compensate the large device drag, the low-profile VG with a much lower device height was introduced by Kuethe (1972). In the investigation, Kuethe focused on resolving the noise issue

9

from unsteady two-dimensional disturbances and unsteady forces on an airfoil in landing phase. A wavy surface with chamfer ends was placed at an angle about 15° with respect to the flow direction near the trailing edge of an airfoil. The surfaces tested were embedded in the turbulent boundary layer with h/δ of about 0.2 - 0.5. The VG with such h/δ was later referred to as a micro-VG, or low-profile VG. The application of the wavy surfaces accomplished a successful reduction in noise by reducing the unsteady forces on the blade, and suppressing the Kármán vortex street over a large range of Reynolds number. Reducing the height of VG could largely reduce the frontal area thus lowering the drag force. The investigation of the flow behind this VG showed that the streamwise vortices generated from the low-profile VG had an appropriate strength, such that it would not affect the downstream flow region after the flow reattached.

The height of the low-profile VGs are typically scaled as $h/\delta \approx 0.2$, and the local velocity at this height is over 75% of the free-stream velocity (Lin, 1999). Further increase of the height only moderately improves local velocity while significantly increases drag (Lin, 1999). Lin et al. (1990; 1990a; 1991) performed a series of experiments on a backward-facing ramp test bed, and observed that the doublet and reverse wishbone VG had the best performance at $h/\delta \approx 0.1$ and $h/\delta \approx 0.2$, respectively. The result from Lin et al. (1990a; 1990b; 1991) and Lin (1999) proved that low-profile VGs, such as reverse wishbone VG and vane-type VG, with $h/\delta \approx 0.2$ were as effective as the traditional large VGs with $h/\delta \approx 0.8$ in delaying the separation.

2.2.6 Vortex generator design criteria

As evaluated by several investigations, the performance of VGs depends on their geometrical parameters such as incidence angle, gap between adjacent vanes, chord length, and device height. The experiment of Godard and Stanislas (2006) on vane-type VGs showed that the optimum incidence angle between the side-edge of the VG and the freestream was about 18°. Betterton et al. (2000) performed an experiment using LDA, and found that the counter-rotating vortices produced by vane VGs with a gap of $1h$ decayed more slowly than the ramp and joined vane VGs without gap. Based on the experimental investigation of Lin (1999) and numerical study of Forster and White (2014), a longer chord is expected to generate stronger vortices. As discussed before, device height was found to be related to the effective range. The effective region will be extended if the size of the VG is larger; this is due to the increase the strength of the vorticies. Hence the individual vortices could persist longer during viscous dissipation.

The effectiveness of a VG also depends on its installation location. A low-profile VG performs best when placed 5-30h upstream of a fixed separation line (Lin, 1999). Based on oil visualization conducted by Lin (1990a), the optimum location to install the doublet and wishbone VGs falls in between 3-10h upstream of the separation baseline. A numerical study of ramp type VGs on a cambered wing by Forster and White (2014) demonstrated that VGs are more effective when placed at the point of maximum velocity.

2.2.7 Vortex structures

Early smoke visualization experiments (Barrett and Farokhi, 1993) showed the generation of counter-rotating vortices in the wake of wedge-element VGs. The mean flow pattern were observed experimentally via two-dimensional LDA (Lin, 1999; Betterton et al., 2000), PIV (Godard and Stanislas, 2006) measurement, velocity probe measurement (Wendt and Hingst, 1994) and numerically (Froster and White, 2014), all of which studying the wake of various V-shape VGs.

In the last several decades, investigations have been limited to one and two-dimensional measurements due to the limitation in measurement technology. With the development of more advanced tomographic PIV (tomo-PIV), the three-dimensional instantaneous wake region can be measured quantitatively. Recent tomo-PIV works conducted by Sun et al (2016) and Ye et al. (2016) visualized and quantitatively studied the hairpin vortices and their evolution within the instantons wake of micro-ramp VG. These investigations motivated further research interest to study hairpin structures from the instantaneous flow field. A detailed investigation of the hairpin vortex generated by a hemisphere in a laminar boundary layer was provided by Acarlar and Smith (1987) to demonstrate the evolution process of hairpin vortex. The hairpin vortex contained a transverse vortex tip, an inclined neck (due to shear layer profile), and a pair of streamwise vortex legs (Acalar and Smith, 1987). The momentum transfer process is driven by the rotation of transverse vortex and streamwise counter-rotating vortex legs; as the legs travel downstream, they undergo a mutual cancellation due to the viscous interaction between two opposite vortex cores, effectively reducing their core vorticity and the corresponding ejection event. The tip will not be affected by this mechanism while it continues to diffuse.

2.3 Measurement method

2.3.1 Particle Image Velocimetry

Particle Image Velocimetry was developed as a non-intrusive optical measurement technique to overcome the disadvantages of traditional intrusive measurement techniques such as hot wire measurements. It also allows the measurement to have a larger field of view, resulting in more advantages compared to LDA measurements (Raffel et al., 2007).

A brief PIV experimental setup is illustrated in the Figure 2.4 to demonstrate the principle of PIV technique.
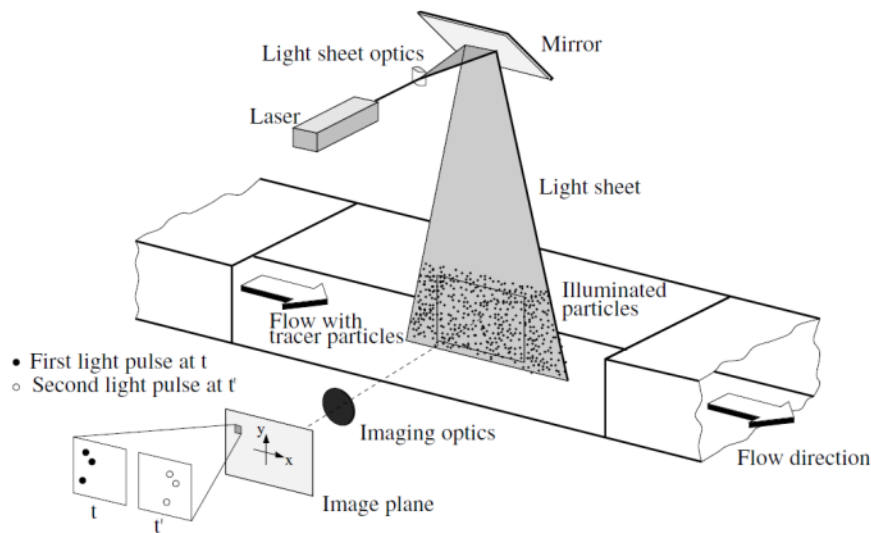
Figure 2.4. Experimental arrangement for particle image velocimetry in a wind tunnel (Raffel et al., 2007).

As shown in Figure 2.4, tracer particles are added into the examined flow, and are illuminated twice within a short time interval. The time interval was defined by the time delay between two laser pulses. The light sheet is generated by a double-pulsed laser through an optical system, which expands the laser beam into a light sheet with desired thickness and size at the proper position. The illuminated particles will be recorded by a recording system consisting of imaging optics and digital cameras. The recorded double-frame images will then be processed using a cross-correlation algorithm between the two frames to obtain the velocity vectors of the tracer particles.

Seeding

Since the measurement is conducted by determining the particle velocity instead of the flow velocity, the mechanical properties of the tracer particles have to be examined (Raffel et al., 2007). Two requirements need to be satisfied when choosing the tracer particles: (1) particles should follow the fluid motion faithfully, and (2) the scatterred light of the particles should be sufficient for the recording devices (Prasad, 2000a).

For the first requirement, the primary source of error is from the inertia of the particle. Assuming the particles have spherical shapes and in a viscous fluid at very low Reynolds number, the behaviour of the tracer particles under acceleration can be derived from Stokes' drag law. The relative motion between particle and fluid to first order is described by Basset (1888), as shown in Equation (2.1)

$$\frac{\pi d_p^3}{6} \rho_p \frac{dU_p}{dt} = -3\pi\mu d_p \left(U_p - U_f\right) \tag{2.1}$$

where U_p is the velocity of the tracer, and U_f is the velocity of the fluid; and μ is fluid dynamics viscosity. The particle diameter is represented as d_p; the density of particle and fluid are ρ_p and ρ_f respectively. The estimation for the velocity lag U_s in a continuously accelerating fluid is therefore equal to

$$U_s = U_p - U_f = d_p^2 \frac{(\rho_p - \rho_f)}{18\mu} \cdot \frac{dU_p}{dt} \tag{2.2}$$

If the particle density is much larger than the fluid density, the step of U_t follows an exponential law

$$U_t(t) = U\left[1 - \exp\left(-\frac{t}{\tau_s}\right)\right] \tag{2.3}$$

with a relaxation time τ_s, shown as

$$\tau_s = d_p^2 \frac{\rho_p}{18\mu} \cdot \left(\simeq \frac{d_p^2}{v}\right) \tag{2.4}$$

The particle behavior described by the above equations only yields when the fluid acceleration is constant or Stokes' drag law applies, for example; the particle Reynolds number is smaller than unity (Melling, 1997). Otherwise, the solution to the particle motion is more complicated (Raffel et al., 2007).

The second requirement states that sufficient light should be reflected to the camera sensor in order to effectively detect the particles. It is more effective and economical to increase the particle intensity by carefully choosing seeding particles (Raffel et al., 2007). The intensity of the light scattered is a function of the particle to fluid refractive index ratio, particle diameter, particle shape, orientation, polarization and observing angle (Raffel et al., 2007). Mie scattering theory is applied when the particles are spherical, with diameter d_p larger than the wavelength of the illumination light source. The light scattering by a 30 μm glass particle in water is shown in Figure 2.5, the distribution shows that forward scattering is more favorable compared to the backward scattering. However, in practice, a 90˚ recording (perpendicular to the light sheet) is more often used due to the limitation in depth-of-field (Raffel et al., 2007). As the Mie scattering diagram shows, the light spreads in all directions. The massive multi-scattering situation is incurred for a heavily seeded flow since the imaged light is from both direct illumination and light scattered by more than one particle. Both increasing the particle diameter and seeding density will improve the scattering efficiency. However, there are also constraints for the suggestions mentioned above, for example; the background noise increases with increase of seeding density. Also, non-uniform particle size makes it harder to determine the effect of simply adding large particles (Raffel et al., 2007).
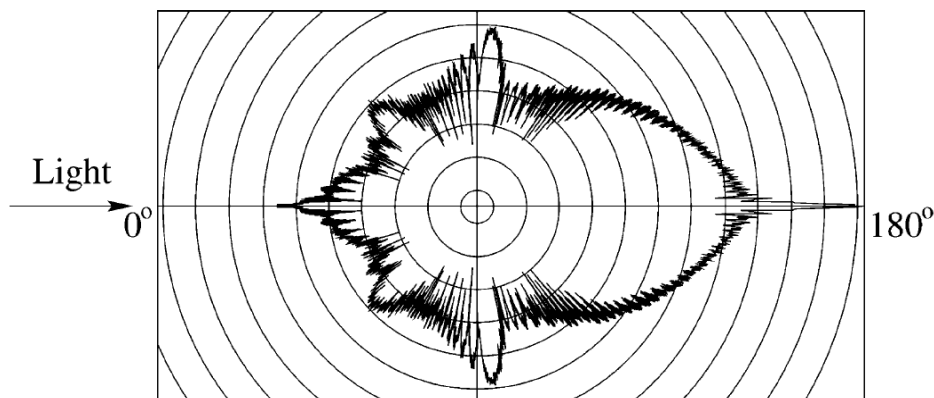
Figure 2.5. Light scattering by a 30 μm glass particle in water (Raffel et al., 2007).

Lasers are usually chosen to be the illuminating source in PIV measurements due to their ability of emitting high energy density monochromatic light (Raffel et al., 2007). It allows the formation of thin light sheets and illuminates the tracer particles at consistent wavelength during recording, which prevents chromatic aberrations. A laser typically consists of three main components: (1) laser material, (2) pump source, and (3) mirror arrangement.

Light source

PIV measurement is usually conducted using continuous wave (CW) lasers or pulsed lasers. Typical CW lasers are argon-ion lasers (gas laser) (Prasad, 2000a). They are frequently used for LDA measurements and can be easily used for low-speed water PIV measurements (Raffel et al., 2007). A generally used pulsed laser in PIV measurement nowadays is Neodym-YAG laser (Nd: YAG laser). It is a four-level (as shown in Figure 2.6b) solid-state laser that generates laser beam by Nd^{3+} ions. The advantage of the four-level system is it requires less pumping power compare to the three-level system shown in Figure 2.6a since the lower energy level E2 stays unoccupied at room temperature, the population inversion is easier to achieve (Raffel et al., 2007).
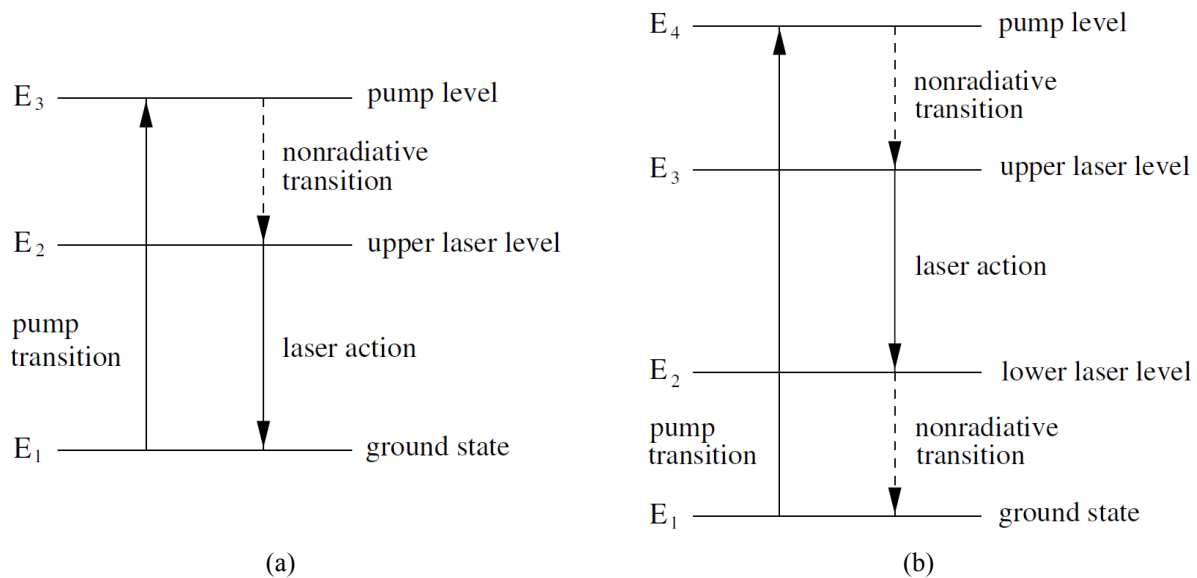
Figure 2.6. Level diagrams of (a) three and (b) four level lasers (Raffel et al., 2007).

The short duration between pulses is the advantage of pulsed laser with double cavity, which allows the capture of very high speed particle motion (Prasad, 2000a).

Recording devices

Typically PIV images are recorded using charge-coupled device (CCD) cameras, which has an electronic sensor that can converts light to electric charge. It has advantages for convenient set ups, fast digitizing and high light-sensitivity (Prasad, 2000a). The operation of CCD pixels is described in Figure 2.7. The CCD sensor consists of a semiconducting substrate with metal conductor surface, an insulating oxide layer, an n-layer (anode) and a p-layer (cathode). As seen in Figure 2.7, when a photon with certain wavelength enters the p-n junction, an electron-hole

15

pair with positive charge is generated; it is known as the photoelectric effect. The electron-hole is absorbed at the p-layer and produces electrons, which moves to the potential well (local minimum) at the center of the pixel due to the gradient of the electric field. The electrons will be stored and accumulated in the potential well while the pixel is continuously exposed to light. This process produces the signal of light intensity for further PIV processing.
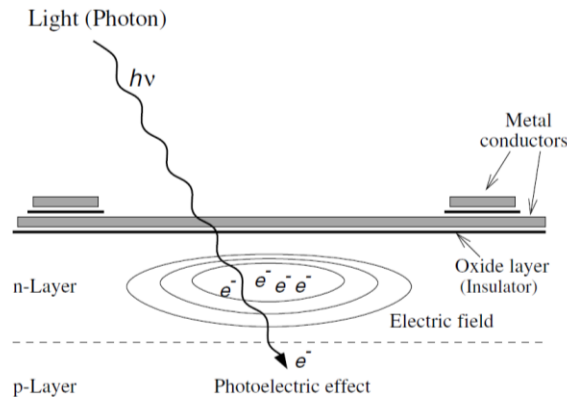
Figure 2.7. Simplified model of a CCD pixel (Raffel et al., 2007).

Cross-correlation in PIV

The concept of cross-correlation of PIV images is described in Figure 2.8 and Figure 2.9. As seen in Figure 2.8, a sampled region $f(m,n)$ from image 1 at time t_0 is cross-correlated with the corresponded sampled region $g(m,n)$ from image 2 at $t_0 + \Delta t$. The sampled region, as known as the interrogation window, is located at (m,n) in pixel unit. The mechanism of the cross-correlation process is explained in Figure 2.9, the pattern of the signal of tracer particles, shown as local peaks from image 1 (Figure 2.9a) and image 2 (Figure 2.9b) are compared to obtained the spatial shift as the velocity vector (Figure 2.9c).
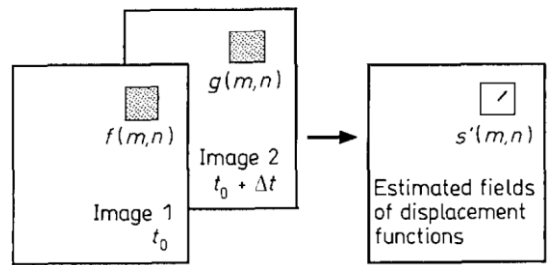
Figure 2.8. Conceptual arrangement of frame-to-frame subsampling associated with digital PIV (Willert and Gharib, 1991).

16

(a)

(b)

(c)
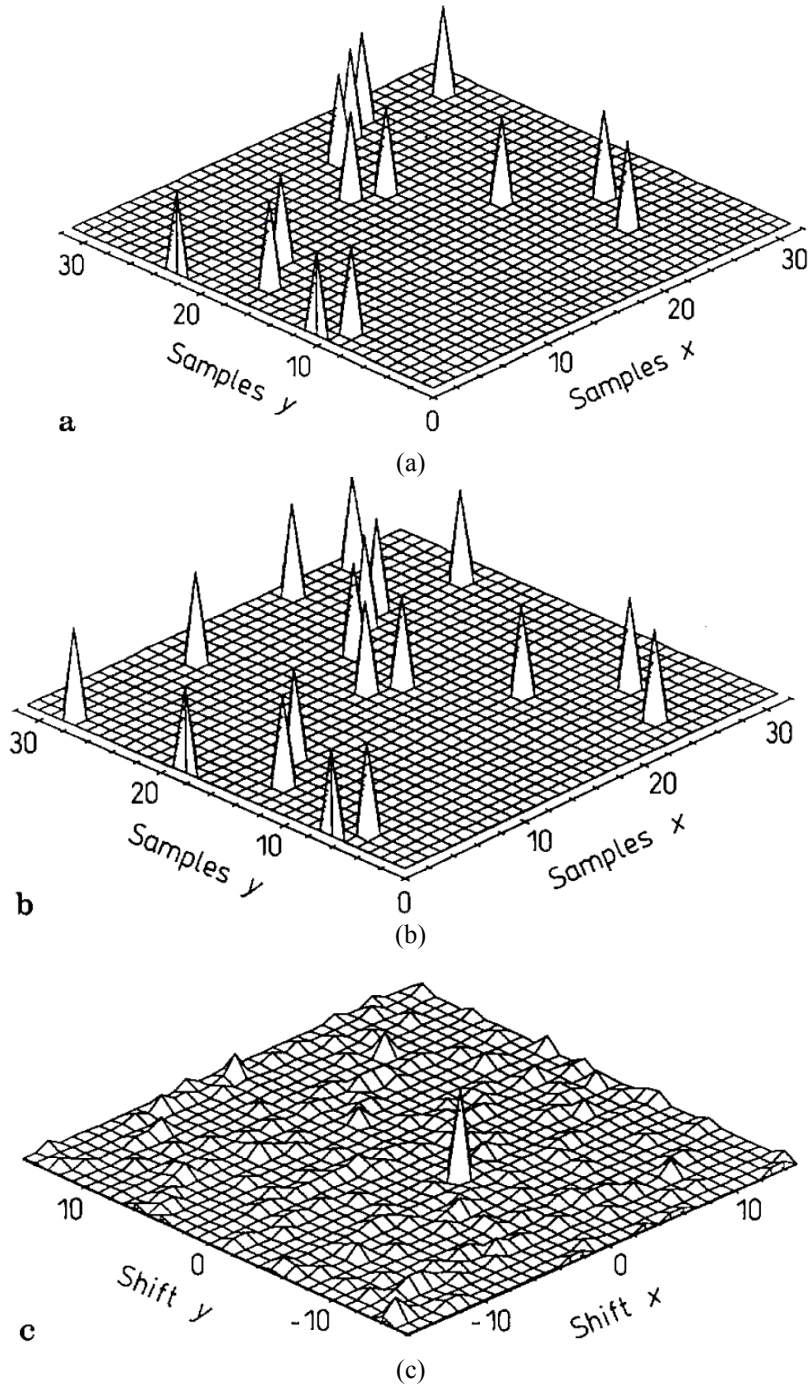
Figure 2.9 Cross-correlation estimate (c) of image pair (a),(b) which consist of randomly positioned particles represented as Dirac delta functions; the relative spatial is -4 pixels along the *Y*-axis (Willert and Gharib, 1991).

2.3.2 Stereoscopic PIV

Stereo-PIV is a 2D-3C system which involves the use of a two camera system. The related engineering applications can be tracked back to several decades ago. The major advantage of the system allows the accurate capture of the third velocity component, the out-of-plane velocity, by

17

correcting the perspective error of a single view through the application of the second camera The stereo-PIV measurement requires the recording system to satisfy the following conditions: the two separate recording devices have to operate simultaneously, and the cameras have to view the same object at different viewing angles (Prasad, 2000b). Most of the stereo-PIV configurations can be classified into two major categories: translation systems and rotational systems (Prasad, 2000b).

The translation system has the axes of the two cameras parallel to each other. For instance, as seen in Figure 2.10a, the two cameras are both orthogonal to the laser sheet, although the magnification of each cameras is not necessary to be the same (Prasad, 2000b). This system has advantages of simplicity, and high image quality due to the absence of refractive index variations. The superposition of the views is therefore easier due to the uniform magnification property (Prasad, 2000b). One drawback of the translation system is the limitation of viewing area stated by Gauthier and Riethmuller (1988); the effective recording area is the common area viewed by each camera. This is addressed by off-setting the sensor's center away from the lens axis as shown in Figure 2.10a, in which the common viewing area is maximized by adjusting the relative distance, D, between camera 1 and camera 2. Another constraint of the translation system is the upper bound of the half viewing-angle θ, as defined in Figure 2.10a. It sets a limitation for the accuracy of the measurement of the out-of-plane velocity component. Prasad and Adrian (1993), Arroyo and Greated (1991), and Soloff et al. (1997) showed that the out-of-plane component error is 3 to 4 times larger than the in-plane component at a viewing angle of 30°.

The rotational systems, however, allow the arrangement of a less restricted viewing angle. As seen in Figure 2.10b, the cameras are rotated towards the object plane, which allows θ to reach a higher angle than the translation systems without lowering the lens performance. The corresponding out-of-plane measurement accuracy is therefore increased. The disadvantage of this arrangement is the non-uniform magnification over the measurement field; distorted images from the co-linear object plane, lens plane, and image plane. The Scheimpflug condition needs to be satisfied to obtain well focused images (Altenhofen, 1952).
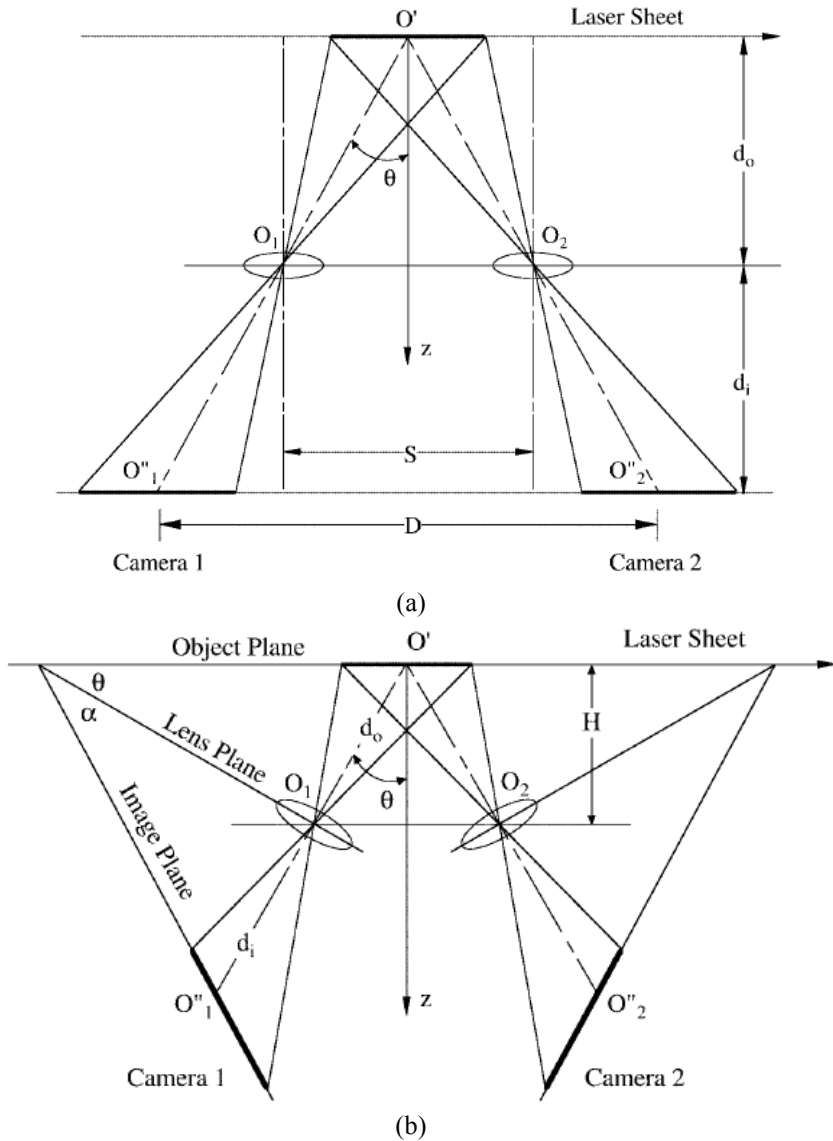
Figure 2.10. Two major stereo-PIV configurations: (a) translation systems, and (b) rotational system. The translation system has the axes of the two cameras parallel to each other (Prasad, 2000b).

Reconstruction is the process of mapping the image planes and object planes and combing the two individually integrated velocity fields from each camera to obtain the three-dimensional velocity field (Prasad, 2000b). There are two methods for this process: (1) geometric reconstruction, and (2) calibration-based reconstruction. There are two types of calibration-based reconstruction: (1) 2D and (2) 3D in which the former is more advanced, and the latter involves unnecessary system geometry rendering.

The standard 2D calibration for stereo-PIV is conducted by transversely moving a planar calibration target with known mark information through the illuminated region (Wieneke, 2008).

Usually multiple calibration images are required to take for different translate stages. The 3D calibration method requires the use of a dual plane 3D calibration target, which the translation of calibration target is not necessary for a thin illuminated sheet. More details about the calibration procedures are discussed in the literatures (Soloff et al., 1997; Prasad, 2000b; Calluaud and David, 2004; Scarano et al., 2005). The 2D calibration method will be processed through camera pinhole model and bundle adjustment fit. For each camera, the mapping relation between space (X, Y, Z) to camera pixel coordinates (x, y) is described by function M as

$$(x, y) = M(X, Y, Z) \qquad\qquad (2.5)$$

The following elements can be the error sources of error for the function M: (1) calibration target with inaccurate known information, (2) uncontrolled plate translation, and other mechanical instabilities of the system (Wieneke, 2008). The mapped volume can show a maximum error above 0.5-2 pixels, which will not be a problem for the 2C vector calculation. Such calibration error of 1 pixel is relatively small compared to the other errors, except in case of the high velocity gradients (Wieneke, 2008).

The translational and rotational misalignment between the defined coordinate system and the actual light sheet is a more significant error to stereo-PIV. The corresponding disparity error ranges in between 5-20 pixels (Wieneke, 2008), which could be 10 times larger than the calibration error. To solve this, the procedure named "self-calibration" was developed (Willert, 1997; Coudert and Schon, 2001; Scarano et al., 2005; Wieneke, 2005). Self-calibration is the process of dewarping the simultaneously recorded images from camera 1 and 2, to the plane $z = 0$ defined by the calibration target. Then cross-correlation will be performed to obtain a disparity map for further correction. The process should be repeated to reduce the disparity vectors, which will be used to align the new defined $z = 0$ plane with the actual light sheet. A disparity map with zero magnitude disparity vectors means the two images are properly matched. The peak of the disparity correlation is proportional to the light sheet thickness; hence the self-calibration method could not function well for thick light sheet or volume (Wieneke, 2008).

2.3.3 Tomographic PIV

Tomo-PIV measurement technique was first implemented in 2005 (Elsinga et al., 2005a), which was later widely applied over a large range of three-dimensional flow problems. The investigation of the complex instantaneous turbulent structures where the flow fluctuates at several length scales is normally conducted through PIV since it has the ability to visualize and quantify the instantaneous flow field (Scarano, 2013). Due to the three-dimensional properties of such complex flows, the full understanding of the problem have to be achieved through a three-dimensional approach, such as tomo-PIV (Scarano, 2013). The term, tomographic PIV, first appeared in the study conducted by Kim and Chung (2004), flow in a nasal cavity was measured through planar PIV using multiple planes. The working principles and applications of the modern tomo-PIV were first demonstrated by Elsinga et al (2005a; 2005b). The initial group of developers, the Aerospace Engineering Department of TU Delft and the German company LaVision provided contribution to continually perfect the application of tomo-PIV in the following years. The investigation of flow is more advanced with the assistance of high speed tomo-PIV techniques. It makes the vortex identification, vorticity dynamics, and pressure investigation feasible through a volume-based measurement (Scarano, 2013).

The principle of tomo-PIV is briefly demonstrated in Figure 2.11. The tracer particles within the measurement volume are illuminated by a pulsed laser, and are recorded by four cameras simultaneously from different viewing angles. The particle spatial distribution is then determined through tomographic reconstruction. The three-dimensional vector field is obtained by cross-correlating the reconstructed volume using selected interrogation volume (Elsinga et al., 2006).

In order to perform tomographic reconstruction, the application of the three-dimensional calibration technique, as known as volume self-calibration, was necessary. Volume self-calibration was stated by Wieneke (2007; 2008) as an essential procedure of correcting the image-to-object space mapping and advancing the tomographic reconstruction methods. The procedure of the volumetric self-calibration was summarized by Wieneke (2008) into nine steps: (1) measuring the positions of 2D particles in all camera images, (2) using triangulation to find the positions of possible 3D particles, (3) dividing the measurement volume into sub-volumes, (4) obtaining 2D disparity map with each sub-volume by plotting the corresponding disparities of all particles, (5) using a set of recorded images from all cameras to obtain a better statistics by

summing the disparity map for each sub-volume, (6) the highest disparity peak is detected for each disparity map as the disparity vector, (7) the disparity vector field shall be validated and optionally smoothed, (8) correcting the mapping function for all the cameras, and (9) repeating the whole procedure to further improve the correction.
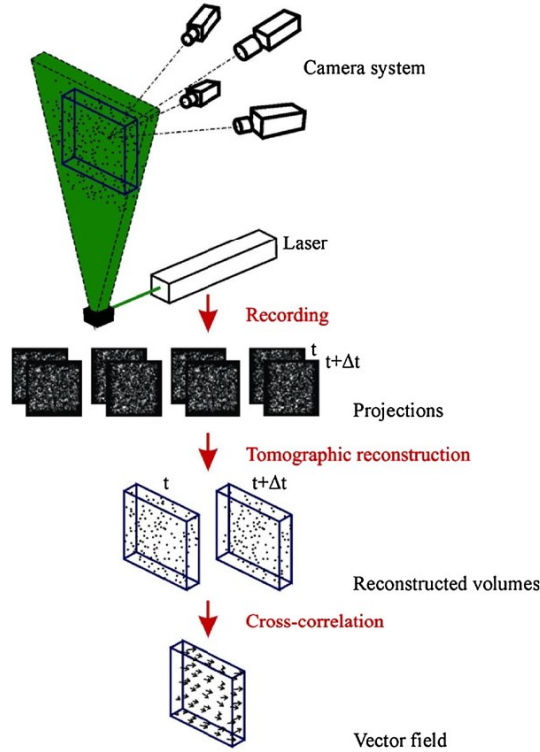
Figure 2.11. Working principle of tomo-PIV (Elsinga et al., 2006).

The discussion of tomographic reconstruction starts with the discretization of measurement volume. As shown in Figure 2.12, the physical space of coordinates (X, Y, Z) is discretized using an array of voxels with intensity $E(X, Y, Z)$ to show the 3D intensity distribution. Equation (2.6) describes the relation between the pixel intensity $I(x_i, y_i)$ and the volume intensity $E(X, Y, Z)$, by projecting the volume intensity on the corresponding i^{th} pixel from the image:

$$\sum_{j \in N_i} w_{i,j} E(X_j, Y_j, Z_j) = I(x_i, y_i) \tag{2.6}$$

where the ith pixel has an intensity value evaluated from N_i number of voxels.

The volume intersection shown in Figure 2.12 is estimated by assuming the line of sight (LOS) as a cylinder and each voxel as a sphere. It avoids the involvement of angular orientation and

leaves the weighting coefficient $w_{i,j}$ to depend on the distance between the LOS and center of voxel, the LOS cylinder diameter (pixel), and the voxel diameter (pixel).
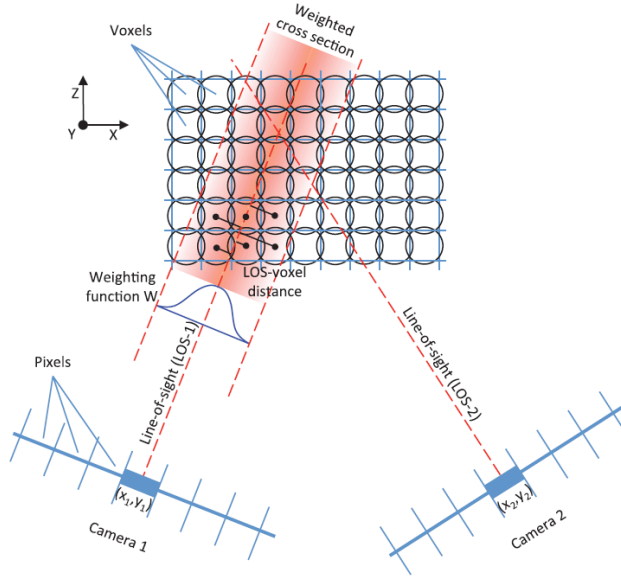
Figure 2.12. Object discretization and imaging model used for tomographic reconstruction. The voxels falling within the shaded stripe (weighted cross section) have nonzero value of the weighting coefficient Wi,j. Spherical shape for voxels is commonly assumed that simplifies the calculation of the weighting coefficient (Scarano, 2013).

Alternate solution approaches to Equation (2.6) are developed as the tomographic reconstruction algorithms. A widely accepted approach is the MART method (Herman and Lent, 1976) with the governing equation defined in Equation (2.7)

$$E_{k+1}(X_j, Y_j, Z_j) = E_k(X_j, Y_j, Z_j) \left(\frac{I(x_i, y_i)}{\sum_{i=1}^{N} W_{j,i} E_k(X_j, Y_j, Z_j)} \right)^{\mu W_{j,i}} \qquad (2.7)$$

where μ is a scalar relaxation parameter between 0 and 1 to ensure the fastest convergence. The MART scheme requires both E and I to be positive. The ratio of the pixel intensity and the corresponding object projection updates the magnitude of the MART scheme. The exponent term, $\mu W_{i,j}$, also agrees with the update of the ith pixel is only affected by $E(X, Y, Z)$.

The major error for tomo-PIV is the inaccurate mapping function M from Equation (2.5) (Wieneke, 2008). The reconstruction of tomo-PIV requires the spatial position of each voxel matches the camera pixel position with the error smaller than 0.4 pixel (Elsinga et al., 2006); Wieneke (2008) suggested a preferred value to be less than 0.1 pixel. Hence in order to

successfully perform the reconstruction, a volume self-calibration is necessary to reduce the mapping function error.

Chapter 3.   Experimental setup

The flow facility and the geometry of the VGs are described in this section. Planar-PIV and stereo-PIV are applied for measurement with high-spatial resolution in a limited number of wake cross-sections. Time-resolved tomo-PIV is applied for volumetric visualization of the wake and evolution of the vortical structures.

3.1.1   Flow facilities

The measurements were conducted in a closed-loop water flume, as shown in Figure 3.1. The test-section is 10-meters-long and has a rectangular cross-section 50 cm high (water level) and 75 cm wide. A flat plate with a half-wedge leading-edge at zero angle-of-attack was installed vertically due to the constraint of image viewing. The gravity is expected to have negligible effect since the region of interest is small The flow speed was set to 0.155 m/s to form a thin laminar boundary layer. The VGs were installed at $l = 65$ mm downstream of the plate leading edge at $Re_l = 10,075$ (based on streamwise location). The corresponding laminar boundary layer thickness is 3.18 mm at this location. The shape factor is also estimated based on the planar PIV measurement of the velocity profile and is 2.8 at this location. The low Re and shape factor indicate a laminar boundary layer immediately upstream of the VG (Schlichting and Gersten, 2016). This allows wake formation without any interaction with vortices from an upstream turbulent boundary layer.

Figure 3.1. The water flume with the flat plate installed vertically at zero angle-of-attack.

3.1.2   Vortex generators

Seven VGs were investigated including both non-conventional and vane-type VGs. The non-conventional VGs are wishbone, doublet, and ramp, as shown in Figure 3.2; and the vane-type VGs are delta VG (DVG), trapezoidal VG (TVG), and rectangular VG (RVG) based on the shape of the vanes, demonstrated in Figure 3.3. The x, y, and z-axis indicate streamwise, wall-normal, and spanwise directions, respectively. The VGs were 3D printed using a transparent resin to prevent strong reflection of the strong laser light. The geometric dimensions including height (h), chord length (c), and incidence angle (β) were kept the same for all VGs. These parameters significantly affect the strength of the generated vortices. Their definition and the corresponding coordinate system are shown in Figure 3.2 and Figure 3.3 for non-conventional VGs and vane-type VGs, respectively. Therefore, to investigate the effect of VG shape on the downstream wake, any scaling effect was prevented. The common dimensions of the VGs are summarized in Table 1. The selected height of the VGs results in a Re_h of 930, which makes the study applicable to unmanned aerial vehicle (UAV) with a cruising speed of up to 10 m/s in air.
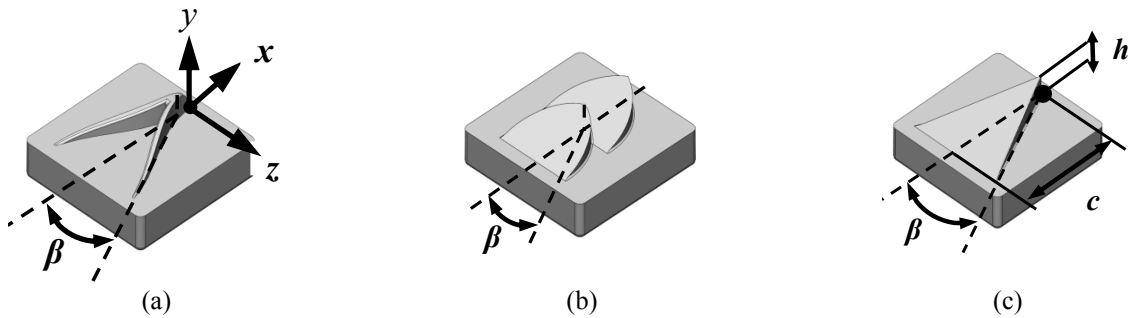
Figure 3.2. The 3D model of (a) wishbone, (b) doublet, and (c) ramp VGs. The supporting surface will be inserted into the flat plate model. The flow is in positive x direction.
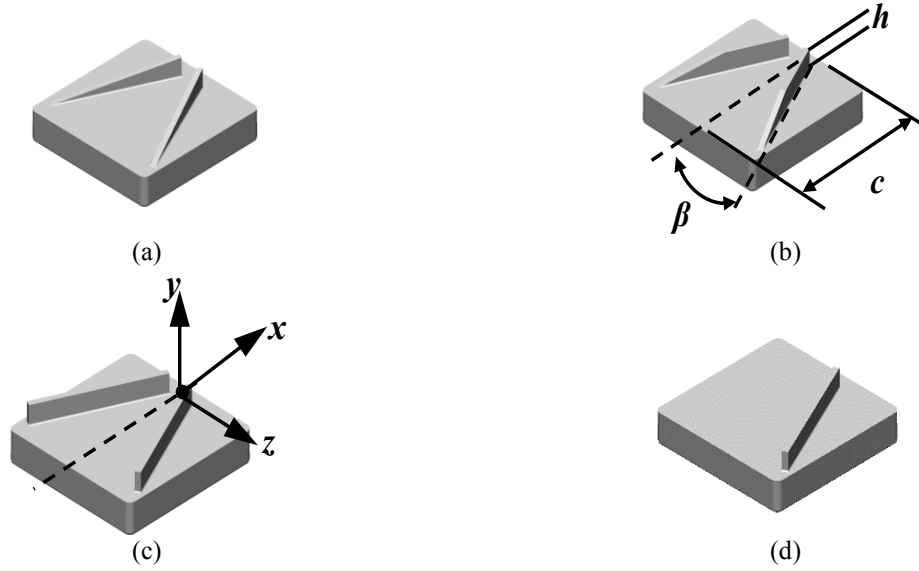
Figure 3.3. 3D model of the VGs with (a) delta, (b) trapezoidal, and (c) rectangular vanes. (d) A single rectangular vane is also investigated for comparison.

Table 3.1. The common dimensions of the VGs

Height (h), mm	Chord length (c), mm	Incidence angle (β), degree
6.0	36.0	25.0

3.1.3 Planar particle image velocimetry

A planar PIV experiment was carried out to measure the 2D flow statistics in an x-y plane along the centerline of the non-conventional VGs, as shown in Figure 3.4. The experiment consisted of an Imager Intense (LaVision GmbH) 12-bit CCD camera with a sensor size of 1040×1376 pix and pixel size of 6.45×6.45 μm^2. The camera was equipped with a Nikon lens with a focal length of $f = 105$ mm at aperture setting of f / 5.6 to image a 44.1×58.3 mm^2 field-of-view (FOV). The digital resolution of the imaging system was 42.4 μm/pix and the depth-of-focus was 3.8 mm. The FOV is specified as FOV1 and shown in Figure 3.4 and is equivalent to $7.35h \times$ $9.72h$ in terms of VG height h. It covers $9.16h$ in the streamwise direction (x) downstream of the VG trailing-edge, and $7.35h$ in the wall-normal direction from the wall surface. A laser sheet with approximately 1 mm thickness was generated using an Nd:YAG laser (Gemini, NewWave Research) with 110 mJ per pulse at 30 Hz. The flow was seeded using silver-coated 2 μm spherical glass beads (SG02S40 Potters Industries) with density of 4 g/cm^3. A set of 1,500 double-frame images were collected for each VG using pulse separation of $\Delta t = 3300$ μs at 5 Hz.

Image pre-processing was conducted to improve the signal-to-noise ratio (SNR) by subtracting the minimum intensity of all the images from each image. The images were also normalized using the ensemble average of all the images. The vector fields were obtained using double-frame cross-correlation with multi-pass algorithm and a final interrogation window (IW) size of 32×32 pixel (1.36×1.36 mm^2) at 75% overlap in Davis 8.3 (LaVision GmbH). The universal outlier detection was applied to remove spurious vectors (Westerweel & Scarano, 2005).
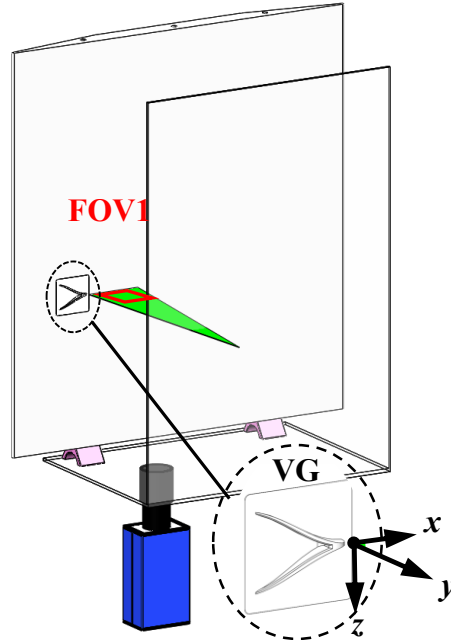
Figure 3.4. A schematic of the camera, laser sheet, VG, and the flat plate for planar PIV measurement. The side and bottom walls of the flume are also shown.

3.1.4 Stereoscopic particle image velocimetry

Stereo-PIV was carried out to characterize the streamwise vortical structures and the vorticity field for the non-conventional VGs with high spatial-resolution in two *y-z* planes across the wake. The stereo-PIV setup consisted of two Image Intense (LaVision GmbH) CCD cameras with solid angle of about 100º with respect to each other, as shown in Figure 3.5. Scheimpflug adapters were equipped to correct the focus planes. Two field-of-views at the upstream and downstream are indicated as FOV2 and FOV3 with dimensions of 35×41 mm^2 ($5.83h \times 6.83h$) at digital resolution of 29.4μm/pix. The camera was equipped with Nikon lenses with $f = 105$ mm at an aperture setting of $f / 11$, which provides depth-of-focus of approximately 8 mm. A laser sheet with 2 mm thickness was formed to accommodate the large out-of-plane motion of

the particles while capturing their smaller in-plane motion in the y and z directions. The same Nd:YAG laser (Gemini, NewAvie Research) and tracer particles were used as were used in the planar-PIV. The initial calibration of the imaging system was performed using a two-dimensional glass sheet with a grid of black circles. The target was imaged at three x locations by moving it ± 0.5 mm with respect to the center of the laser sheet (y-z plane at $x = 0$). The mapping of the calibration image was carried out using a third order polynomial in Davis 7.4 (LaVision GmbH). A set of 1,500 images was collected for each VG at a frame rate of 5 Hz and laser pulse separation of $\Delta t = 1000$ µs. The self-calibration procedure was carried out following Wieneke (2008) in Davis 8.3 (LaVision GmbH) with a root-mean-square (RMS) fit of 0.74 pixels. The SNR of the images was improved by subtracting the minimum intensity of the ensemble of images from each image and normalizing the images using the ensemble average in Davis 8.3. Vector fields were obtained using stereoscopic cross-correlation with multi-pass algorithm and a final IW size of 32×32 pixel (0.94×0.94 mm^2) at 75% overlap. Images were post-processed using universal outlier detection to remove spurious vectors (Westerweel & Scarano, 2005).
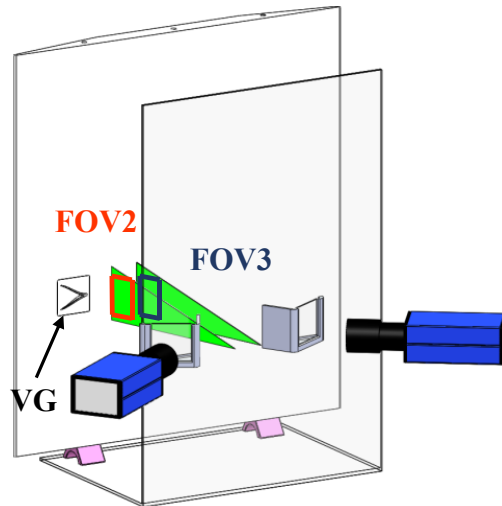
Figure 3.5. The relative location of the two cameras, laser sheet, VG, and the flat plate in stereo-PIV measurement. Two laser sheets are labeled as FOV2 and FOV3 behind the VG.

3.1.5 Tomographic particle image velocimetry

The three-dimensional organization of vortices in the wake of all VGs and their temporal evolution was characterized using tomo-PIV. The tomo-PIV system consisted of four v611 Phantom cameras imaging the illuminated volume in an arrangement shown in Figure 3.6a and b. Each camera has a sensor size of 1280×800 pix with pixel size of 20×20 µm^2. The cameras

were equipped with Scheimpflug adapters and Nikon lenses with focal length of $f = 105$ mm. The apertures were set to $f / 16$ for all cameras with an estimated depth-of-field of 14 mm. The viewing angle between left and right cameras was 60° while the viewing angle between top and bottom cameras was about 40°. Due to the large viewing angle between left and right cameras, two glass prisms were installed to improve the image quality. An Nd:YLF (Dual-head DM20-527DH, Photonics Industries) with 20 mJ per pulse at 1 kHz was used to form a collimated laser sheet. The sheet was 13 mm thick in the y direction and 90 mm wide in x direction. To obtain a top hat intensity profile, the low intensity boundaries of the laser sheet were cropped using knife edges. As seen in Figure 3.6c, the laser sheet was offset by 2 mm from the surface of the flat plate to prevent the strong laser reflection from the flat plate, the plate is highlighted using red solid line, and the illuminated volume is enclosed by yellow lines. The light volume covers 2 mm to 15 mm (2.5h) from the wall surface. The flow was seeded using hollow glass spheres (20 μm) that have a density around 1 g/cm^3 (110P8, Potters Industries).

The measurement volume was 92×55×13 mm^3 (15h × 9h × 2.5h), which is equivalent to 1421 × 848 × 200 voxel in the x, z, and y direction, respectively. This corresponds to a digital resolution of 64.9 μm/pix (magnification of 0.3). The seeding density was approximatlye 0.02 particles per pixel (ppp). The particle size was visually inspected and is around 2-4 pixels (diameter). The initial calibration of the four cameras was carried out using a 3D calibration target (type 11, LaVision GmbH) by fitting a third order polynomial function. The initial disparity map showed a large image distortion with 1-3 pixels residual. After applying the self-calibration, the residual RMS reduced to 0.03 pixels, which is lower than Wieneke's (2008) suggestion of 0.1 pixels.

A total of 3,500 time-resolved images were collected for each VG at a recording rate of 800 Hz. The frame rate allowed small particle displacement of 2-3 pixels between frames in order to apply multi-frame correlation technique. To improve the SNR, the minimum intensity of all the images was subtracted from each image, and the images were also normalized using an ensemble average of all the images. Further improvement was applied to the images by subtracting local minimum and normalizing intensity using a local average with a kernel of 100 pixels. The measurement volume was reconstructed using MART algorithm, (Elsinga, Scarano, Wieneke, & van Oudheusden, 2006) in Davis 8.4 (LaVision, GmbH). Multi-frame cross-correlation was applied to calculate the vector fields using the volume deformation iterative multi-grid technique

(VODIM) developed by Scarano and Poelma (2009). The vector information was obtained through the sliding-average of the correlation maps of three pairs of consecutive frames with Δt = 3.75 ms (equivalent to 267 Hz) to increase SNR. The final window size is 32 × 32 × 32 voxel size (2.08 × 2.08 × 2.08 mm^3) with 75% overlap.

(a)

(b)

(c)

31
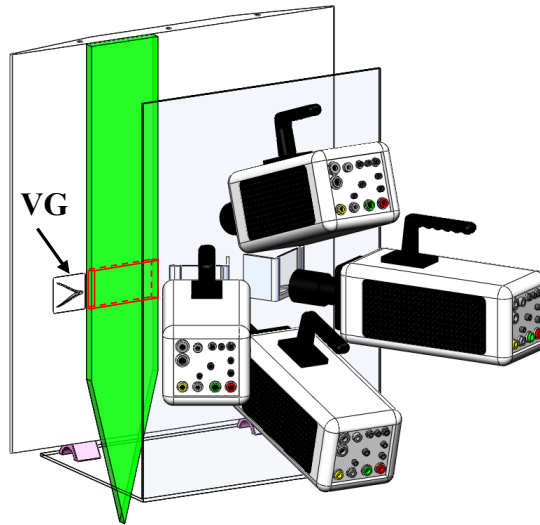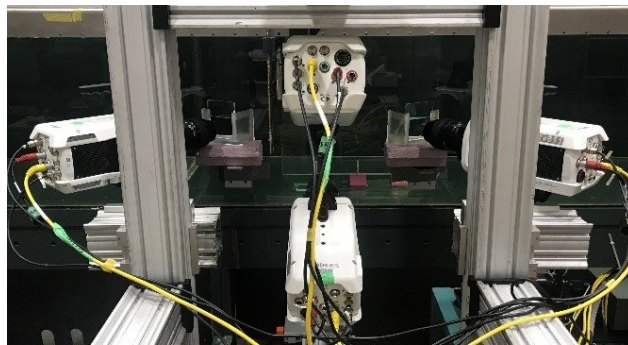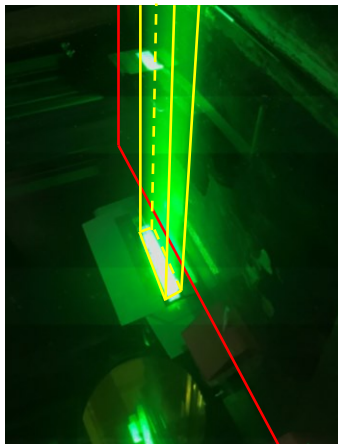
Figure 3.6. (a) A schematic of the configuration of the cameras, glass prisms, illuminated volume, VG, and the flat plate in tomo-PIV measurement. (b) A photo of the experiment showing the high-speed camera configuration with a solid-viewing angle of 40° between the top and the bottom cameras, and 60° between the left and the right cameras. (c) The illuminated volume which has 2 mm offset from the plate.

Chapter 4.   Non-conventional VGs

4.1 Introduction

Vortex generators based on a wedge-element profile were introduced by Wheeler (United States of America Patent No. 4455045, 1991a; United States of America Patent No. 5058837, 1991b) and are referred to as non-conventional VGs in this study. The most common non-conventional VGs are known as the doublet (United States of America Patent No. 4455045, 1991a), wishbone (United States of America Patent No. 5058837, 1991b), and ramp. They were designed to produce stronger vortices than the vane-type VGs in order to provide sufficient flow mixing with a lower device height. Hence the flow separation can be effectively controlled with low device drag.

Previous studies reveal that the dominant vortical structure in the wake of V-shape VGs is a pair of counter-rotating streamwise vortices. For instance, early smoke visualization showed that, in the wake of wedge-element VGs, a pair of streamwise counter-rotating vortices is generated (Barrett and Farokhi, 1993). The same flow pattern has also been observed in the wake of various VGs in V-shape configuration through Laser Doppler Anemometry (LDA) (Betterton et al., 2000; Lin, 1999), two-dimensional PIV (Godard and Stanislas, 2006), velocity probe measurements (Wendt and Hingst, 1994) and numerical simulation (Froster and White, 2014).

Due to measurement limitations, in the last several decades, the major focus has been on characterization of two-dimensional mean flow profiles and the coherent structures have been rarely investigated. With the development of tomo-PIV, the three-dimensional instantaneous wake region can be measured quantitatively. For example, the tomo-PIV measurements conducted by Sun et al (2016) and Ye et al. (2016) captured the hairpin vortex and its evolution within the instantaneous wake of micro-ramp VGs in a supersonic turbulent boundary layer and an incompressible transitional wake, respectively.

Here we investigate the near wake region of three non-conventional VGs with wishbone, doublet, and ramp shapes installed in a thin laminar boundary layer. The objective is to characterize turbulence statistics and the three-dimensional coherent structures of the wake flow. Planar particle image velocimetry and stereo-PIV are applied to characterize the velocity, the Reynolds stresses, and the vorticity fields with high spatial-resolution in several planes across the wake region. The spatial organization of the generated vortical structures and the temporal evolution of the vortical structures are investigated using tomo-PIV. The results identify the mixing mechanism and the effect of each VG shape on the flow development.

4.2　Results and discussion

This section characterizes the wake flow of the three non-conventional VGs by investigation of the mean flow, Reynolds stresses, turbulence production, vorticity field, and the dominant coherent structures. The instantaneous streamwise, wall normal, and spanwise velocities are indicated by *U, V*, and *W*. The time-averaged quantities are specified by *< >* while the fluctuating terms are indicated by lower case letters.

4.2.1　Error analysis for tomo-PIV

The principle of mass conservation is used to evaluate the quality of tomo-PIV measurement (Zhang et al., 1997). The divergence of velocity should satisfy Equation (4.1) everywhere for an incompressible flow.

$$\frac{\mathrm{d}\langle U \rangle}{\mathrm{d}x} + \frac{\mathrm{d}\langle V \rangle}{\mathrm{d}y} + \frac{\mathrm{d}\langle W \rangle}{\mathrm{d}z} = 0 \tag{4.1}$$

To evaluate how well the data satisfies Equation (4.1), the ratio η is computed using Equation (4.2) for each voxel (Zhang et al., 1997). The velocity gradients are interpolated using the second order central difference scheme.

$$\eta = \frac{\left(\frac{\mathrm{d}\langle U \rangle}{\mathrm{d}x} + \frac{\mathrm{d}\langle V \rangle}{\mathrm{d}y} + \frac{\mathrm{d}\langle W \rangle}{\mathrm{d}z} \right)^2}{\frac{\mathrm{d}\langle U \rangle^2}{\mathrm{d}x} + \frac{\mathrm{d}\langle V \rangle^2}{\mathrm{d}y} + \frac{\mathrm{d}\langle W \rangle^2}{\mathrm{d}z}} \tag{4.2}$$

The ratio η is expected to vary between zero and unity, such that $\eta = 0$ indicates Equation (4.1) is well satisfied and $\eta = 1$ represents *<U>, <V>* and *<W>* are independent (Zhang et al., 1997). The distribution of η is given in Figure 4.1. The histogram shows a similar distribution result with the non-filtered experimental data obtained by Zhang et al. (1997). The space-averaged η is 0.384. More discussion from Zhang et al. (1997) states that increasing the correlation window size and applying spatial filter will further improve the quality of vector fields, while at an expense of lowering the spatial resolution and changing the vortex structure, respectively.
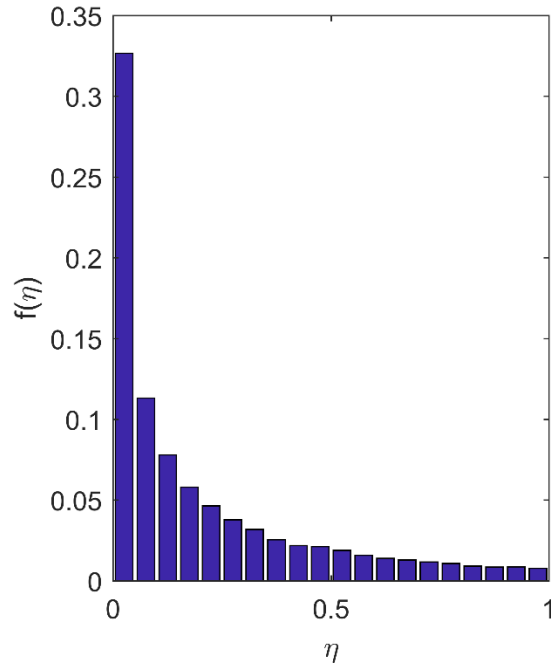
Figure 4.1. Histogram of the distribution of η for tomo-PIV measurement. More than 61% voxels have an η value less than 0.225.

4.2.2 Velocity deficit of the wake

The three-dimensional mean velocity from tomo-PIV measurement in the immediate wake of the three VGs is shown in Figure 4.2. The values of $<U>$ and $<V>$ are normalized by the free stream velocity U_∞. The trailing-edge of the VG is located at $x = 0$. The mean streamwise velocity component is presented using an iso-surface of $0.9U_\infty$ (yellow, light gray) to visualize the boundaries of the wake region. The wall-normal velocity components $<V>/U_\infty$ are also shown using two isosurafces of positive and negative $0.1U_\infty$ indicated by green (medium gray) and blue (dark gray), respectively. The thresholds are selected to visualize the shape of the wake and the wall-normal transport of fluid. The iso-surfaces of streamwise velocity show that the doublet VG has the widest wake in the spanwise direction. The top side of the iso-surfaces in the y-direction are cropped at $y = 2.5h$ due to the limited measurement. However, the cropped area shows that the wake of wishbone and doublet VG is farther extended in the wall-normal direction. In overall, the comparison of wake sizes suggests that doublet VG has the largest pressure drag due to the larger region with velocity deficit. All three VGs generate a consistent upward flow along the centerline of the wake as shown by green (medium gray). The wishbone VG generates the largest region of upward motion while the ramp VG has the smallest region of upward motion.

35

The downward velocity forms two streamwise regions elongated on the two sides of the FOV as shown by the red iso-surfaces (dark gray). The downward velocity at $0.5U_\infty$ persists over a longer distance in the wake of wishbone VG. Therefore, more mixing between the free stream and the low momentum near wall region occurs in the wake of wishbone VG.

(a)   (b)   (c)
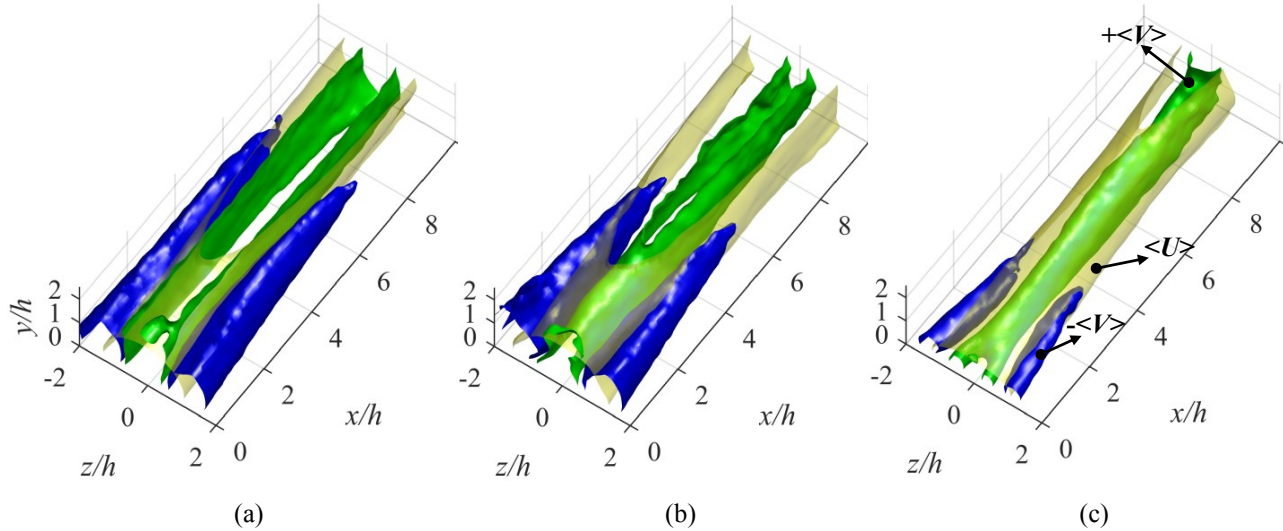
Figure 4.2. Mean velocity in the wake of (a) wishbone, (b) doublet, and (c) ramp VGs. The yellow iso-surface (light gray) shows streamwise velocity of $<U> = 0.9U_\infty$. The green (medium gray) and red (dark gray) isosurafces show $<V> = + 0.1U_\infty$ and $- 0.1U_\infty$, respectively. There are two extended regions with negative wall-normal velocity (red, dark gray) in the wake of wishbone VG, indicating more mixing. The doublet VG has the largest wake deficit region (yellow, light gray).

The distribution of mean streamwise velocity normalized using U_∞ from planar PIV in the *x-y* plane and from stereo-PIV in two *y-z* planes is shown in Figure 4.3. Since the flow is symmetric along the *x-y* plane at $z = 0$, the y-z planes from stereo-PIV is only shown for $z \geq 0$. The planar PIV data and stereo-PIV data approximately match in the interface of the measurement planes. The observation from the *x-y* planes showed that the wishbone VG has the fastest velocity recovery. The velocity from *x-y* plane of the wishbone wake recovers to $0.6U_\infty$ at $y \approx 0.6h$ after $x \approx 1h$. While in the wake of doublet and ramp VGs, the recovery to $0.6U_\infty$ cannot be clearly observed. Therefore, the velocity recovery in the wake of doublet and ramp VG is slower compared to velocity recovery in the wake of wishbone VG. The height of wake, visualized by $0.8U_\infty$. contour level, behind wishbone and doublet VG grows from $1.5h$ to $2.5h$ within streamwise distance of $5h$. However, the height variation in the wake of ramp VG is much smaller, it reaches $1.8h$ at $x = 5h$. This result is close to the observation from the micro-ramp study performed by Ye et al. (2016), which has a similar Reynolds number ($Re_h = 1120$). In their

investigation, the height of wake behind the micro-ramp reaches $y = 2h$ at $x = 5h$. The y-z plane contours show the existence of local minimum streamwise velocity at about $z = 0.5h$ crossing through $x = 2.5h$ in all the cases. The y-z contours also reveal that the local minimum in wake of the wishbone and doublet VGs is lifted as the flow moves downstream and is at higher y/h location in the y-z plane crossing through $x/h = 5$. The contours show that doublet and ramp VG decelerate the flow more than the wishbone VG due to their larger wetted area.
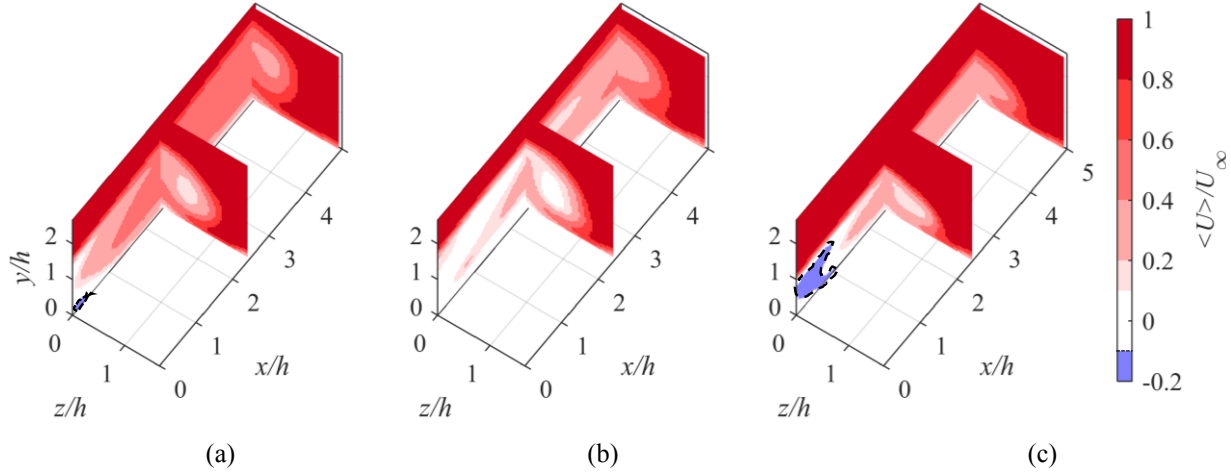
Figure 4.3. Mean streamwise velocity normalized by the free-stream velocity as $<U>/\ U_\infty$ in the wake of (a) wishbone, (b) doublet, and (c) ramp VG. The iso-surfaces shows that the doublet and ramp VGs have a larger velocity deficit while the velocity recovery is faster in the wake of wishbone VG within $x = 0$ to $5h$.

The one-dimensional profiles of velocity deficit (U_{def}) in the wake of three VGs versus the streamwise distance are shown in Figure 4.4 for comparison of wake recovery. The local minimum streamwise velocity $<U>_{min}$ is determined at the upper infection point along the centerline of the wake region The estimated $<U>_{min}$ is used to calculate the velocity deficit as $U_{def} = 1 - <U>_{min}/U_\infty$ and plotted versus x in Figure 4.4. The flow recirculates in the immediate downstream of the doublet and ramp VG. Therefore, $U_{def} > 1$ at $x = 0$-$1.8h$ for the doublet and ramp VG. The velocity deficit recovers quickly to 40% of the free stream velocity in the range $x = 0$-$2h$ behind the wishbone VG. The rate of recovery significantly decreases at $x = 2h$ and the velocity deficit stays around $0.55 U_\infty$ until $x = 5.4h$. It is also observed that the wishbone and ramp VG generate a smoother recovery trend compared to the doublet VG. There is a secondary peak in the velocity deficit of the doublet VG at $x = 4h$, which is associated with second half-body of the double VG. A power law fit cannot precisely characterize the velocity recovery effect at this near wake region of $x < 8h$. However, it could well describe the recovery trend at

farther downstream locations of $x = 7\text{-}27h$ in the investigations of Sun et al. (2016) and Ye et al. (2016) behind the ramp VGs.
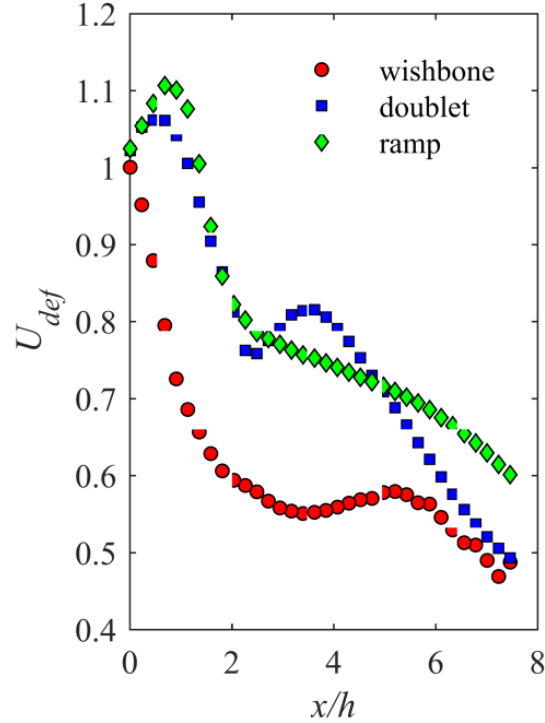
Figure 4.4. Normalized velocity deficit in the wake of VGs along $z = 0$. The wake of wishbone VG has the most rapid velocity recovery to 0.4 U_∞ within $x = 0\text{-}2h$ while the ramp has the slowest. The doublet VG reaches a similar recovery (≈ 0.4 U_∞) at $x \approx 6h$ with a local peak at about $x = 4h$.

The mean wall-normal velocity contours for all the VGs are normalized using U_∞ and are presented in Figure 4.5. A scaling factor of $\times 2$ is applied to all the y-z planes for better visualization of the weaker downward velocity. As seen in the x-y planes in Figure 4.5, the wishbone VG presents the strongest upward motion, which confirms the observation based on tomo-PIV in Figure 4.5. The most significant upward flow transport for the wishbone VG happens within $x = 1 - 4h$ with a velocity peak of $0.5U_\infty$. This strong wall-normal behaviour persists over a longer streamwise distance compared to the two other VGs. The doublet VG has the second strongest upward flow motion, however, the peak positive $<V>$ magnitude is 1.6 times weaker than the wishbone VG at $x = 2.5h$. The ramp VG shows the weakest upward flow motion. The positive $<V>$ has a magnitude between 0.1 and 0.2 U_∞, which is negligible

compared to the wishbone VG. The *y-z* planes from Figure 4.5 show that the wishbone VG has the strongest downward flow motion. The ranking of the extent of downward flow transport is the same as the upward. The strongest downward motion appears at *z* = 1*h* for all cases, and it is weaker compared to the upward motion. In general, the extent of wall-normal fluid transport decreases as the flow travels downstream.

The contours of Figure 4.6 show the mean spanwise velocity *<W>* from stereo-PIV in the two *y-z* planes. The pattern of the spanwise motion is consistent with the vortex direction inferred from the wall-normal velocity contours. The wishbone VG has the strongest spanwise motion, followed by the doublet VG. The ramp VG produces the weakest spanwise motion. The dominant spanwise motion is the rotating motion toward the centerline of the wake at the near-wall region, and outward from the centerline at farther away from the wall. The wishbone VG presents a strong inward velocity of $0.2U_\infty$ at *x* = 2.5*h*, and remains strong at *x* = 5*h*. The doublet VG shows a similar strong inward velocity pattern. The ramp VG is much weaker compared to the other two VGs. The upper outward motion is generally weaker compared to the inward motion, and decades at farther downstream.
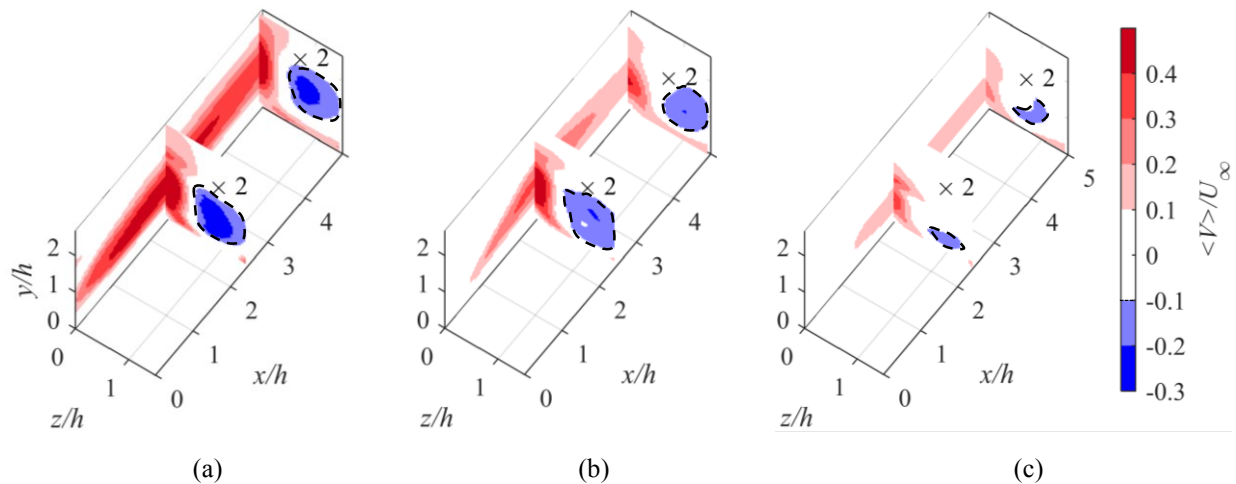
Figure 4.5. Mean wall-normal velocity normalizing based on the free-stream velocity as *<V>*/ U_∞ for (a) wishbone, (b) doublet, and (c) ramp VG. The contours show that the wishbone VG produces the largest wall-normal motion within the measured domain. The contours of the *y-z* plane are multiplied by 2 for better visualization. The negative contours are enclosed by the dash lines.
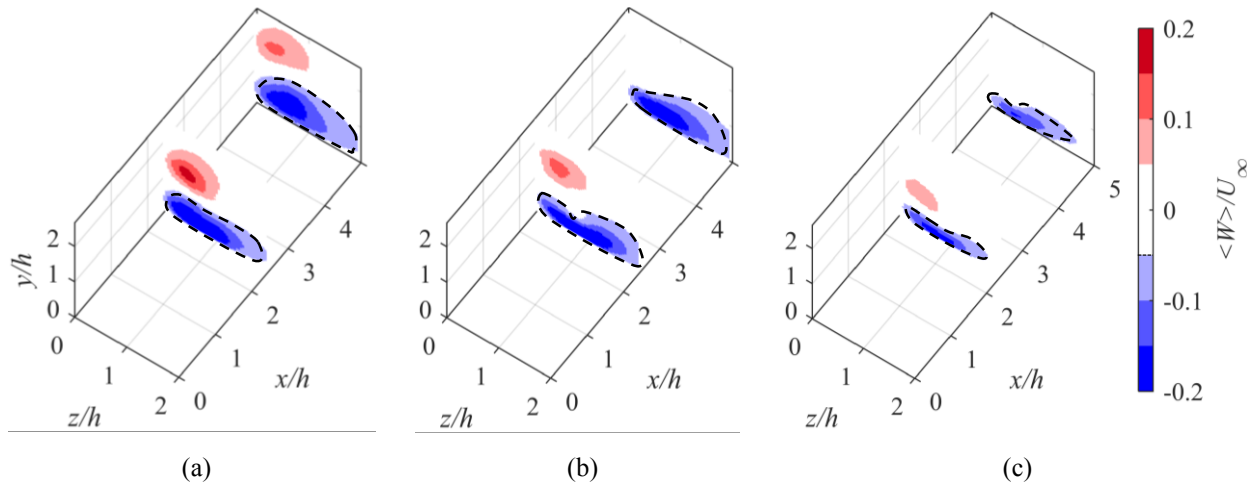
Figure 4.6. Mean spanwise velocity contours normalized with free stream velocity $<W>/U_\infty$ for (a) wishbone, (b) doublet, and (c) ramp VG. Inward velocities tend to be larger than outwards. The wishbone VG has the strongest spanwise behavior. The negative contours are enclosed by the dash lines.

The measurement of mean velocity (shown in Figure 4.5 and Figure 4.6) in the wake of three VGs showed that a pair of steady streamwise counter-rotating vortices are generated. This pair of vortices has also been observed in the previous literatures. The LDA measurement of Betterton et al. (2000), showed the same pattern in the wake of ramp VG. The numerical simulation using shear stress transport model conducted by Forster and White (2014) also shows the similar pattern behind a ramp like VG. In the experiment of Barrett and Farokhi (1993), the flow over the wishbone, ramp and doublet VG was visualized using titanium tetrachloride smoke filaments. The shedding of two counter-rotating vortices could be observed when the flow passes over the VGs from the planar and stereo-PIV measurement. The vortex core location is determined by observing the intersection region of low wall-normal and spanwise velocity contours. The vortex cores appear to be at $(y, z) = (1h, \pm 0.5h)$ in the $x = 2.5h$ plane, and at $(y, z) = (1.5h, \pm 0.5h)$ in the $x = 5h$ plane behind the wishbone and the doublet VG. In the wake of ramp VG, the vortex cores are closer to each other and closer to the wall. The center of the vortex is at $(y, z) = (0.5h, \pm 0.2h)$ of $x = 2.5h$ and at $(y, z) = (1h, \pm 0.2h)$ of $x = 5h$ in the wake of ramp VG. The observation also shows no obvious widening of the distance between the pair of the vortices in z direction within the range $x = 0$ to $5h$. The pattern indicates vortex cores are lifting due to the self-induced velocity, which explains the increase in the height of the wakes in the contours of the streamwise velocity profiles. The stronger upward motion relative to the downward velocity is caused by the focused ejection event induced by the mutual effect of two counter-rotating streamwise vortices

described by Acalar & Smith (1987).The doublet VG is expected to cause the largest parasitic drag based on the size of the wake region. The wishbone VG is more efficient in enhancing the flow mixing due to stronger streamwise vortices and fastest recovery of the wake deficit.

4.2.3 Coefficient of drag

The drag coefficient C_D of each VG was evaluated at $x = 5h$ to study the adverse effect of installing VG. The conventional approximation equation considers only the streamwise momentum flux through the control surface (y-z plane). However, as reported by Ramamurti and Sandberg (2001), the thrust values obtained through finite element flow solver were significantly lower than the cases computed with conventional method (Koochesfahani, 1989). A more complete equation, which considers the streamwise velocity fluctuation and downstream pressure deficit (Bohl and Koochesfahani, 2009), was derived as:

$$C_D = -\frac{2}{c} \iint \left\{ \frac{\langle U \rangle}{U_\infty} \left(\frac{\langle U \rangle}{U_\infty} - 1 \right) + \varepsilon \left(\frac{\langle U \rangle}{U_\infty} - 1 \right) + \left(\frac{u_{rms}}{U_\infty} \right)^2 - \left(\frac{v_{rms}}{U_\infty} \right)^2 + \frac{1}{2} \left(1 - \frac{U_0^2}{U_\infty^2} \right) \right\} dydz \quad (4.3)$$

where $\langle U \rangle$ and U_0 are the mean streamwise velocity and the free stream velocity at the control surface respectively. The free stream velocity upstream the VG is shown by U_∞. The term $\varepsilon(\langle U \rangle/U_\infty-1)$ is added to represent the effect of variation of $\langle U \rangle$ along control surface, where ε is computed as $0.5-U_0/U_\infty$. The term u_{rms} and v_{rms} are the velocity fluctuation in x and y direction respectively. The effect of pressure deficit is represented by the last two terms, derived from the y-component of mean Navier-Stokes equation, and Bernoulli's equation (Bohl and Koochesfahani, 2009). The integration is carried out over a control surface that covers from -3h to 3h, and 0 to 6h in the z and y direction respectively. The calculated C_D is shown in Table 4.1, with information of wetted area and frontal area. The VG wetted area is only the surface area of the VG body; the total wetted area includes both the surface area of VG and the wall area too. The doublet VG produces the largest drag, followed by the wishbone and the ramp VGs. No direct correlation between C_D and wetted area can be observed. For example, the C_D of the doublet VG is 15.4% more than the wishbone VG while the total wetted area is only differenced by about 0.05%; the ramp VG has a smaller C_D, however, it has a larger VG wetted area. Since the frontal area is also the same for all the VGs, the difference in C_D for non-conventional VGs is believed to be caused by the difference in wake size. It agrees with the observation from Figure 4.2.

Table 4.1. C_D for different non-conventional VGs at $x = 5h$

VG	VG Wetted Area(mm^2)	Total Wetted Area(mm^2)	Frontal Area(mm^2)	C_D
Wishbone	560	1989	108	0.0097
Doublet	1060	1993	108	0.0112
Ramp	850	1875	108	0.0064

4.2.4 Reynolds stresses

The normal Reynolds stresses in the wake of VGs are investigated here to characterize the strength of turbulence fluctuations. The Reynolds stresses are an indication of unsteadiness in the wake and small-scale mixing. The fluctuating velocity u are obtained by decomposing the instantaneous velocity U, e.g. $U = <U> + u$. The contours of streamwise component of normal Reynolds stress, $<u^2>$, normalized by U_∞^2 from planar and stereo-PIV are shown in Figure 4.7. As shown in the x-y planes, the peak of $<u^2>/U_\infty^2$ appears at the shear layer between the upper wake and the free-stream for all the VGs. The high intensity layer of $<u^2>/U_\infty^2$ for the wishbone and doublet VGs thickens rapidly after $x \approx 2.5h$, while the ramp VG has a consistent thin layer of high intensity $<u^2>/U_\infty^2$ along the whole x-axis range. The magnitude of $<u^2>/U_\infty^2$ in y-z planes increases from $x = 2.5h$ to $5h$ for all the VGs. The doublet VG has the strongest $<u^2>/U_\infty^2$, followed by the wishbone VG. The ramp VG has a negligible $<u^2>/U_\infty^2$ in the y-z plane at $x = 2.5h$ and no contour is visible.

(a)   (b)   (c)
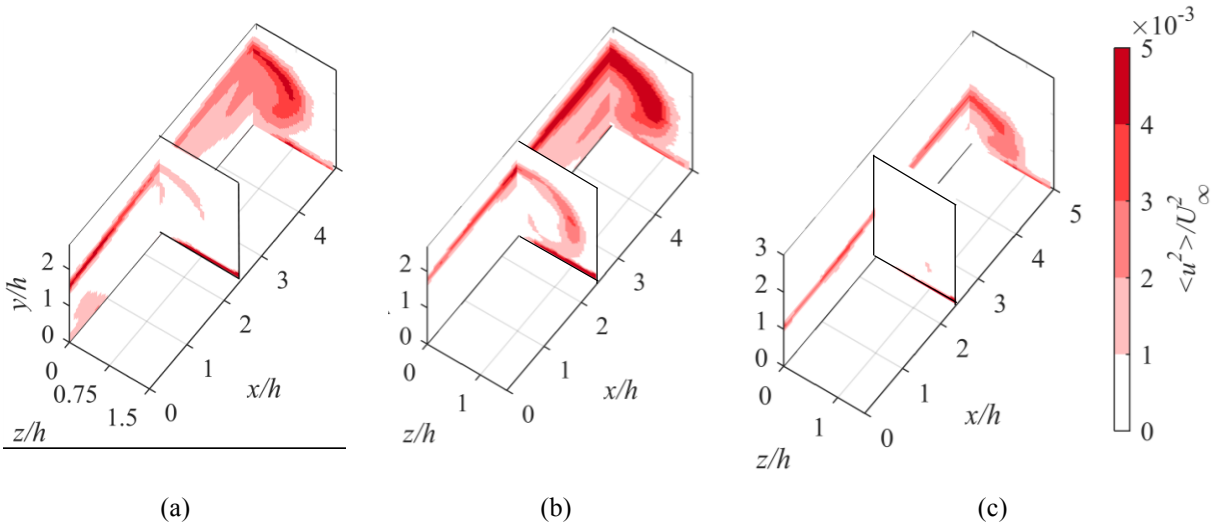
Figure 4.7. The streamwise Reynolds stress $<u^2>/U_\infty^2$ for (a) wishbone, (b) doublet, and (c) ramp VG. The doublet VG has the strongest $<u^2>/U_\infty^2$ in the wake region.

The wall-normal Reynolds stress $<v^2>$ normalized by U_∞^2 is presented in Figure 4.8. The $<v^2>$ is relatively weak in the near wake region as observed in the x-y plane from planar-PIV. In the

wake of wishbone and the doublet VGs, a significant $<v^2>/U_\infty^2$ does not appear until $x = 2h$. For the ramp VG, $<v^2>/U_\infty^2$ in the x-y plane is not visible until farther downstream at $x = 4h$. The high intensity $<v^2>/U_\infty^2$ layer for all the VGs grows thicker and becomes stronger with increase of streamwise distance. The $<v^2>/U_\infty^2$ in y-z planes at $x = 2.5h$ is relatively weaker compared to the one shown in x-y planes. Therefore, to better visualize the distribution of $<v^2>/U_\infty^2$, a scaling factor $\times 3$ is applied to the y-z planes for all three VGs. As observed in the y-z plane at $x = 2.5h$ from the wake of wishbone VG, the high intensity $<v^2>/U_\infty^2$ tends to be concentrated in the shear layer between the wake and the free stream. At the same location in the wake of doublet VG, the large $<v^2>/U_\infty^2$ appears at the shear layer above the wake, and a spot near the wall. At $x = 2.5h$, no significant $<v^2>/U_\infty^2$ can be observed in the wake of ramp VG except at the shear layer close to the wall. The pattern of $<v^2>/U_\infty^2$ in the y-z planes at $x = 5h$ is visualized without applying a scaling factor for all the VGs. Similar to the result observed in Figure 4.8, the doublet VG presents the most intense $<v^2>/U_\infty^2$, and the ramp VG shows the smallest $<v^2>/U_\infty^2$. It represents the doublet VG has the strongest small-scale turbulent mixing in wall-normal direction
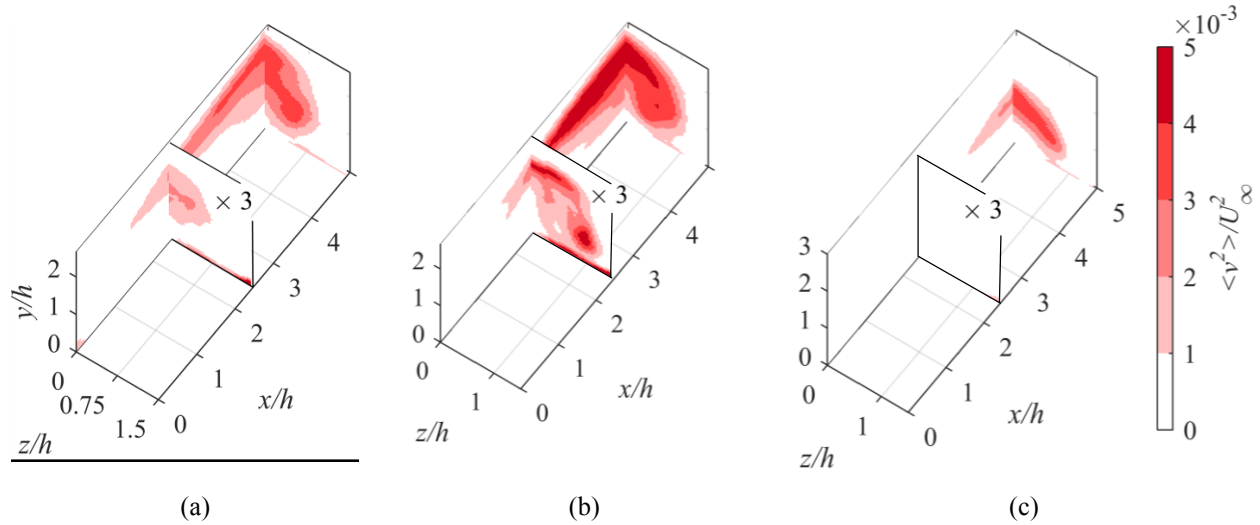
Figure 4.8. The wall-normal Reynolds stress $<v^2>/U_\infty$ for (a) wishbone, (b) doublet, and (c) ramp VG. The doublet VG has the strongest $<v^2>/U_\infty^2$. The contours of the y-z plane at $x = 2.5h$ are multiplied by 3 for better visualization.

The Reynolds shear stress $<uv>$ normalized by U_∞^2 is shown in Figure 4.9 to investigate the correlation of the streamwise and wall-normal velocity fluctuation. The regions with negative $<uv>/U_\infty^2$ have a major role in production of turbulence. From the observation of the x-y planes, the largest negative $<uv>/U_\infty^2$ is observed at the upper interface of the wake and the free-stream (i.e., shear layer). The doublet VG presents the most intense negative Reynolds shear stress. It is

created by the ejection and sweep events induced by the counter-rotating vortices. The negative $<uv>/U_\infty^2$ layer in the wake of wishbone and doublet VG starts more upstream than the ramp VG. To analyze the pattern from the *y-z* planes, a scaling factor ×3 is applied to the *y-z* planes at $x = 2.5h$ due to the relatively small magnitude of $<uv>/U_\infty^2$ at this location. A spanwise layer of negative $<uv>/U_\infty^2$ is observed at $y = 2h$ in the wake of wishbone and the doublet VGs. Note that in the wake of ramp VG at $x = 2.5h$, no $<uv>$ could be detected even after applying the scaling factor. Within the *y-z* planes at $x = 5h$, the negative $<uv>/U_\infty^2$ region expands and the magnitude gradually intensifies in all the VG cases. The doublet VG generates the strongest negative $<uv>/U_\infty^2$ while the ramp VG has the weakest negative $<uv>/U_\infty^2$. It is also noticed that a positive $<uv>/U_\infty^2$ region is presented below the core of the streamwise vortex. This is associated with dominant motions form the first and third quadrant of velocity fluctuations (i.e., *v* versus *u*).
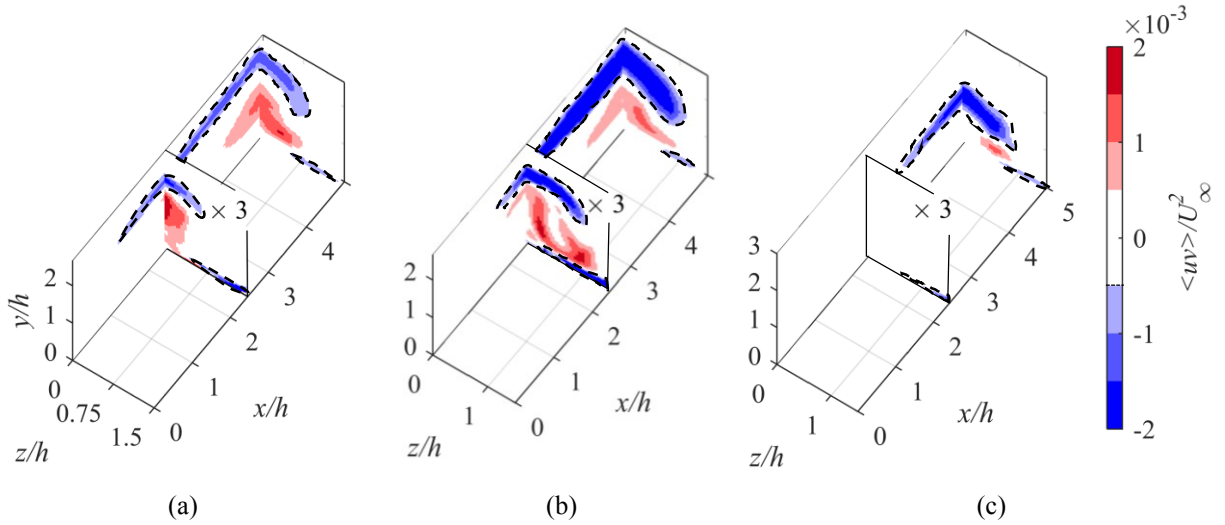
Figure 4.9. Reynolds stress $<uv>/U_\infty^2$ for (a) wishbone, (b) doublet, and (c) ramp VG. The doublet VG generates the highest level of turbulence as indicated by its strong negative $<uv>/U_\infty^2$ in all presented planes. The contours of the *y-z* plane at $x = 2.5h$ are multiplied by 3 for better visualization. The negative contours are presented within the dash lines.

4.2.5 Turbulence production

The production of turbulence kinetic energy is investigated to determine the ability of the VG in extracting energy from the mean flow. The produced small-scale turbulence is expected to enhance small-scale mixing and contribute to the effectiveness of the VG. The production of turbulence $<P>$ is expressed in Equation (4.4).

$$\langle P \rangle = -\left[\langle u^2 \rangle \frac{d\langle U \rangle}{dx} + \langle v^2 \rangle \frac{d\langle V \rangle}{dy} + \langle w^2 \rangle \frac{d\langle W \rangle}{dz} + \langle uv \rangle \frac{d\langle U \rangle}{dy} + \langle uv \rangle \frac{d\langle V \rangle}{dx} + \langle uw \rangle \frac{d\langle U \rangle}{dz} + \right.$$
$$\left. \langle uw \rangle \frac{d\langle W \rangle}{dx} + \langle vw \rangle \frac{d\langle V \rangle}{dz} + \langle vw \rangle \frac{d\langle W \rangle}{dy} \right].$$

(4.4)

Due to the highly three-dimensional property of the turbulence production, the production terms are obtained from tomo-PIV measurement. The high noise drawback of tomo-PIV is also being lowered by averaging the flow field from 3,500 snapshots and using the second order central difference scheme to calculate the velocity gradients.

The turbulence production contours for the three VGs are shown in Figure 4.10 after being normalized by U^3/h. Three different levels of threshold are selected to demonstrate the variation of the production intensity within the measurement volume. The production contour in red (dark gray) has a threshold of 0.05, the orange (medium gray) contour has a threshold of 0.03, and the yellow (light gray) contour is constructed using a threshold of 0.01. Due to the measurement volume limitation in y-direction, the contours are cropped in y-direction after $x = 2.5h$ for the wishbone and doublet VG since they have larger wake region. As seen in Figure 4.10a, the largest production behind the wishbone VG is concentrated along the centerline of the wake region within $x = 0\text{-}1.5h$. Most of the production stays at the shear layer between the upper interface of the wake and free-stream. The intensity of production gradually decreases in both spanwise and streamwise direction. The observation of Figure 4.10b shows that the pattern of the doublet VG is similar to the wishbone VG, except the most intense production region persists farther till $x = 2.6h$. The contour from Figure 4.10c illustrates that the ramp VG has a much weaker turbulence production in terms of both iso-surface size and intensity compared to the other two VGs The results show that the doublet VG extracts more turbulent kinetic energy from the mean flow. It also agrees with the large streamwise and wall-normal Reynolds stresses observed in the wake of doublet VG in Figure 4.7 and Figure 4.8.
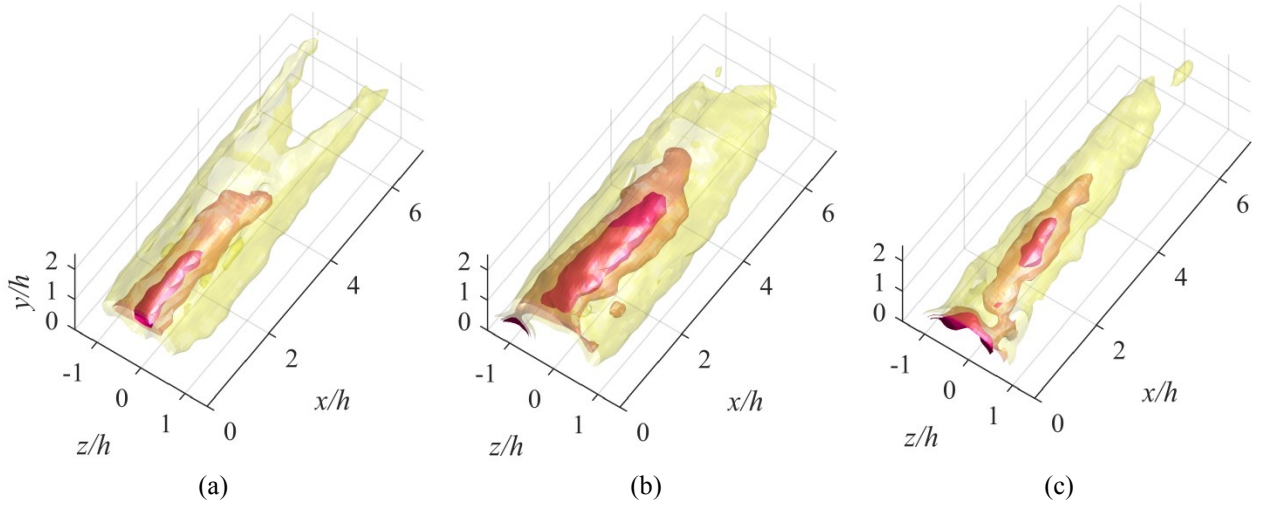
Figure 4.10. Normalized turbulence production $<P>/(U_\infty^3 h)$ for (a) wishbone, (b) doublet, and (c) ramp VG, obtained from 3,500 time-resolved tomo-PIV reconstructed volumes. The iso-surfaces thresholds are 0.05, 0.03, and 0.01, which correspond to red (dark gray), orange (medium gray), and yellow (light gray) respectively The doublet VG shows the strongest turbulence production.

4.2.6 Vorticity field

The streamwise vortex in the VG wake is visualized using the normalized mean streamwise vorticity $<\Omega_x>/(U_\infty^2/h^2)$ iso-surfaces shown in Figure 4.11. The positive streamwise vorticity is rendered in yellow (light gray) with a threshold of 0.015, and the negative streamwise vorticity is shown in red (dark gray) with a threshold of -0.015. A pair of counter-rotating vortex tubes is observed in the wake of all the three VGs. With the increase in the streamwise distance, the diameter of the vorticity tubes gradually reduces for all the VGs, which represents that the vortices become weaker. In the wake of wishbone VG shown in Figure 4.11a, the vortices are close to each other. The same pattern is also observed in the near wake region of the doublet VG from Figure 4.11b. However, as shown in the wake of ramp VG from Figure 4.11c, the spanwise gap between the vortices is much larger. It is believed such difference is created by the difference in VG geometry. The difference shows that the tail trailing-edge of the wishbone VG and the second half wedge body of the doublet VG are responsible for forming the vortices close to the centerline without leaning towards each other. Overall, the wishbone VG produces the strongest steady vortex pair in the mean flow field, followed by the doublet, and the ramp VG.

46
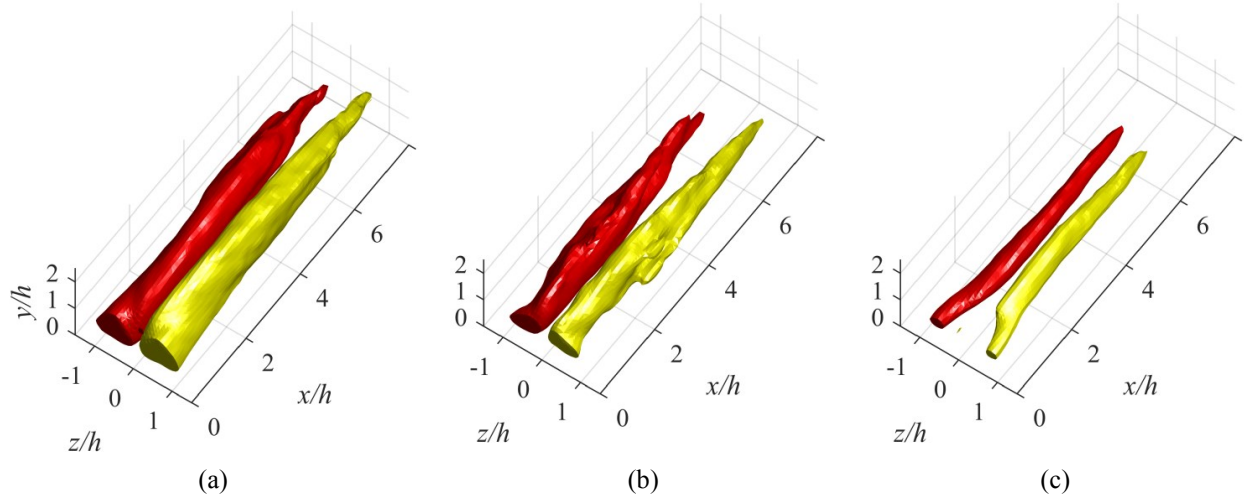
Figure 4.11. Mean streamwise vorticity $\langle\Omega_x\rangle/(U_\infty^2/h^2)$ iso-surfaces with thresholds of $\langle\Omega_x\rangle/(U_\infty^2/h^2) = 0.015$ in yellow (light gray), and $\langle\Omega_x\rangle/(U_\infty^2/h^2) = -0.015$ in red (dark gray) for (a) wishbone, (b) doublet, and (c) ramp VG. The wishbone VG produces the strongest counter-rotating vortices.

The time-averaged square of vorticity fluctuation $\langle\omega_x^2\rangle$ and $\langle\omega_z^2\rangle$ are normalized with U_∞^2/h^2 and are shown for the wishbone, doublet, and ramp VGs in Figure 4.12a, b, and c, respectively. The $\langle\omega_x^2\rangle$ and $\langle\omega_z^2\rangle$ are measured using stereo-PIV and planar-PIV in y-z and x-y planes, respectively. All VGs show a strong vorticity fluctuation at the shear layer formed between the upper wake and the free-stream in the x-y plane. The strength of this vorticity fluctuation layer gradually decreases with increase of streamwise distance. The $\langle\omega_z^2\rangle/U_\infty^2/h^2$ from the wake of doublet and ramp VGs is generally larger than the $\langle\omega_z^2\rangle/U_\infty^2/h^2$ from the wake of wishbone VG. The pattern showed that the intensity of the transverse vorticity fluctuation is proportional to the VG wetted area. Meanwhile, the observation of the y-z contours shows a different result, such that the wishbone VG produces the strongest $\langle\omega_x^2\rangle/U_\infty^2/h^2$. The high intensity distribution of $\langle\omega_x^2\rangle$ for the ramp VG is concentrated close to the wall while for the wishbone and double VGs large $\langle\omega_x^2\rangle$ is also observed at the center of vortex. As the flow progresses from $x = 2.5h$ to $x = 5h$, the $\langle\omega_x^2\rangle/U_\infty^2/h^2$ produced by the wishbone VG is weakened. The similar trend of decay is observed in the wake of doublet VG. In the study performed by Ye et al. (2016), the $\langle\omega_x^2\rangle/U_\infty^2/h^2$ will continuously increase after $x = 5h$. Wishbone VG is inspected to shed the strongest streamwise vortices which also persist the longest within the investigated wake region ($x = 0$-$5h$).
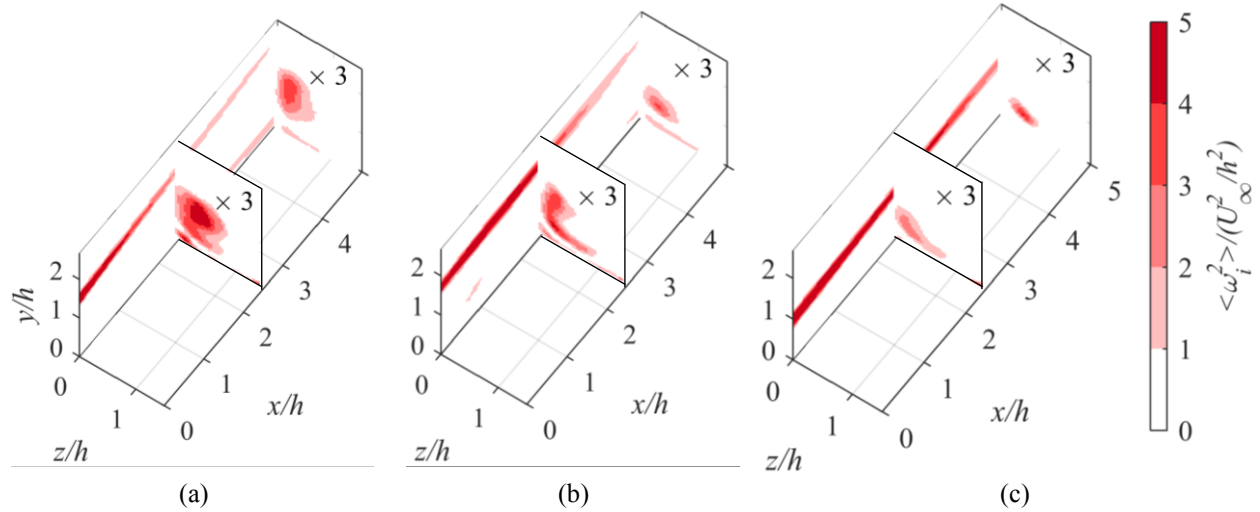
Figure 4.12. The time-average of square of spanwise vorticity fluctuation $<\omega_z^2>$ is measured using planar PIV and is shown in x-y plane after being normalized by U_∞^2/h^2. The time-average of square of streamwise vorticity fluctuation $<\omega_x^2>$ is measured using stereo-PIV, and is shown in y-z planes after being normalized by U_∞^2/h^2. A scaling factor of ×3 is applied to all y-z planes. The contours are shown for the (a) wishbone, (b) doublet, and (c) ramp VGs. Wishbone VG shows the strongest streamwise vorticity fluctuation.

4.2.7 Three-dimensional flow visualization

Proper-Orthogonal-Decomposition (POD) of the three-dimensional fluctuating velocity fields from tomo-PIV is carried out using the snapshot POD method (Lumley, 1967; Sirovich, 1987) to remove the small-scale turbulence. The energy distribution of the POD modes also indicates the contribution of larger structures to the wake development. The percent of turbulent kinetic energy of each mode relative to the total turbulent kinetic energy for each VG is shown in Figure 4.13a. The distribution of the energy of the modes for the doublet VG is very broad. However, for the wishbone and ramp VG, the first two modes contain most of the energy. As seen in Figure 4.13b, about forty percent of the total energy is stored in the first 12 and 14 modes for the ramp and wishbone VG, respectively. The doublet VG needs 18 modes to reach the same energy level. The difference in energy distribution reveals that the doublet VG produces more small-scale turbulence in its wake, which matches the result that it has the highest level of turbulence within its wake region. The animation, Supp_Video_S2.avi, of the instantaneous flow field of the doublet VG also justifies this by showing the small-scale turbulence structures in the wake region.
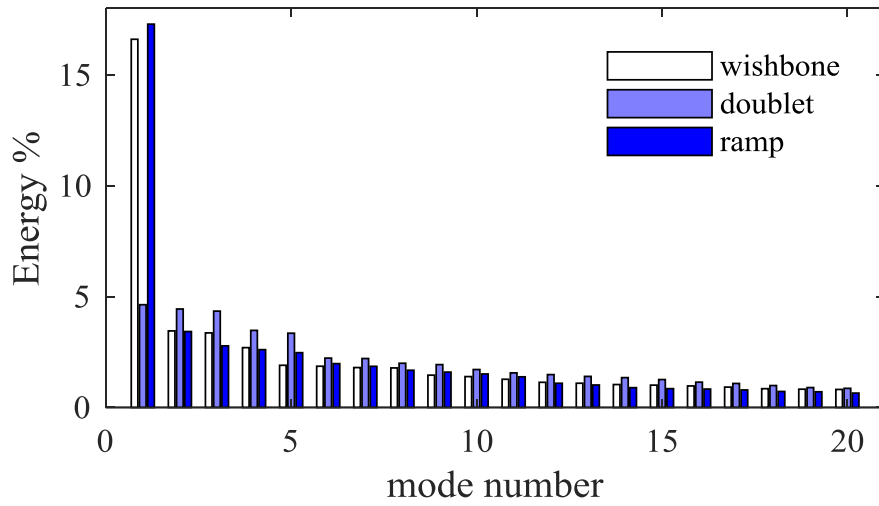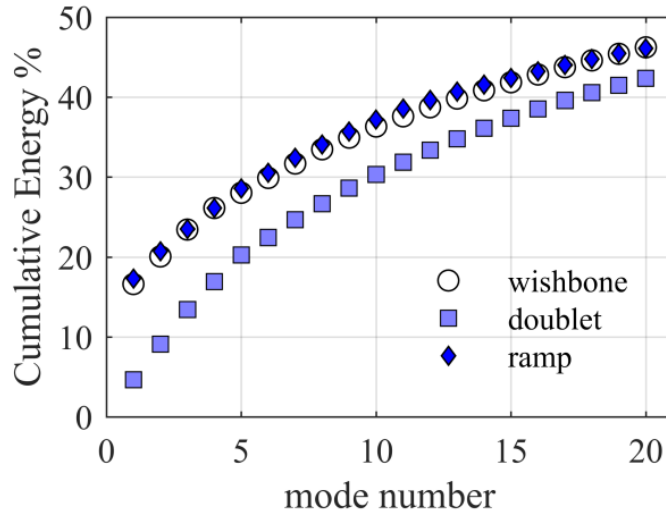
Figure 4.13. (a) The distribution of turbulent kinetic energy of the POD modes, and (b) cumulative energy distribution of the first 20 POD modes for all VGs. The POD analysis is carried out on 3,500 time-resolved snapshots. The energy of the POD modes of the doublet VG has broad distribution while the first POD mode of the wishbone and doublet VG form a large percentage of the total turbulent kinetic energy.

The dominant coherent structures of the instantaneous flow field are reconstructed using 40% of the cumulative energy and are shown in Figure 4.14. This POD reconstruction filters out small-scale turbulence and measurement noise. Increasing the energy level to a higher level does not change the shape of dominant coherent structure. The visualization of the vortical structures is carried out using Q-criterion (Kolář, 2007; Hunt, Wray, & Moin, 1998) as shown with yellow color (light gray). The figures also show iso-surfaces of wall-normal fluctuating velocities with v

> 0 and v < 0 in green (medium gray) and blue (dark gray), respectively. The fluctuating wall-normal velocity indicates the strength of the velocity (ejection or sweep) induced by the tip of the hairpin vortex and its direction of rotation. The shedding of hairpin vortex structures could be obviously seen in all three flow fields. In the wake of wishbone VG, a pair of strong streamwise vortices is observed close to the wall. As seen in the animation, Supp_Video_S1.avi, the steady vortices lasts till around $x = 5h$ at the selected threshold $Q = 100$ s^{-2}. The threshold for the wall-normal fluctuating velocities has a magnitude of $v = 0.01$m/s. Different from the pattern shown in the mean flow field, hairpin vortex appears to be the dominant coherent structure in the instantaneous flow field. The hairpin tip is cropped as the structure moves downstream due to the limitation of the measurement volume in y-direction. From the animation, the transverse hairpin tip is formed at the immediate downstream of the trailing-edge, it then connects to the steady vortices to form the hairpin neck. Also, as seen in Figure 4.14a, the hairpin vortex cannot be detected after $x = 6h$ due to the rapid drop in vortex strength. In the wake of doublet VG, coherent vortex structures is illustrated using a threshold of $Q = 100$ s^{-2}. The wall-normal fluctuating velocities are presented with the same level of thresholds as in the wishbone VG case, $v = \pm 0.01$m/s. The original vortex pair generated by the first half-body may interact with the vortical structure induced by the second half-body. As a result, the interaction weakens the steady streamwise vortex pair (see Supp_Video_S2.avi) and presents a broad distribution of mode energy. As shown in Figure 4.14b, the hairpin vortex is more unstable with irregular shape compared to the other two cases. Similar to the case of wishbone VG, the hairpin vortex from the wake of doublet VG is cropped in y-direction with the increase in streamwise distance, and it cannot be detected as it moves beyond $x = 6h$. The evolution of the hairpin vortex from the wake of ramp VG is presented in Supp_Video_S3.avi. The magnitude of the Q-criterion, and wall-normal fluctuating velocity thresholds are 20 s^{-2} and 0.01 m/s, respectively. A pair of streamwise steady vortices could be observed within the near wake region, close to the wall. As shown in Figure 4.14c, the hairpin vortices show a good coherency in terms of both strength and shape such that they can still be detected even after $x = 6h$. However, the height of the hairpin vortices from the wake of ramp VG is about the half height as the ones from the wake of wishbone and doublet VGs, so that the measurement volume cropping issue is not encountered.
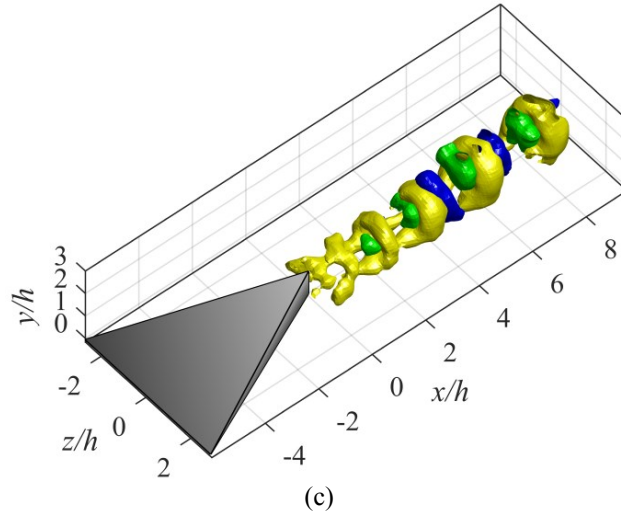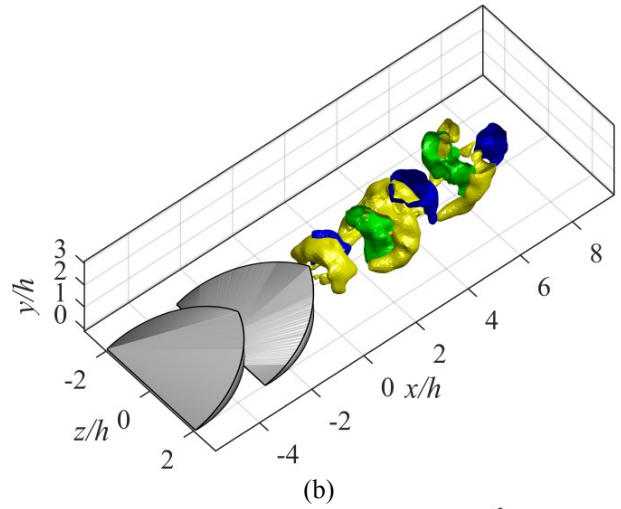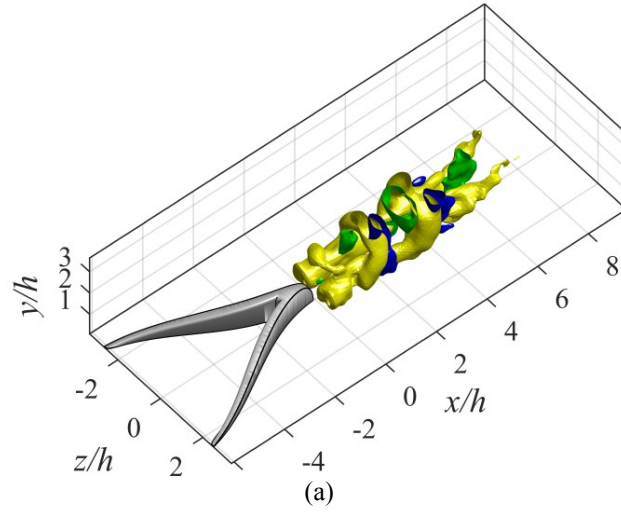
Figure 4.14. Visualization of coherent structure using Q-criterion (yellow, light gray), and wall-normal fluctuating velocity ($v > 0$: green, medium gray; $v < 0$: blue, dark gray) for (a) the wishbone (threshold: $Q = 100$ s^{-2}, $v = \pm 0.02$ m/s), (b) the doublet (threshold: $Q = 100$ s^{-2}, $v = \pm 0.02$ m/s), and (c) the ramp VG ($Q = 20$ s^{-2}, $v = \pm 0.01$ m/s).

51

Overall, the coherent vortex structures from the wake of wishbone and doublet VGs present much stronger vortices, which indicates a more efficient wall-normal flow exchanging compared to the ramp VG. The generated vortex structures are relatively small compared to the size of the VG, which matches the observation of the wake size from Figure 4.2. It suggests that the non-conventional VGs has a significant effect in controlling the wake induced device drag. The existence of the strong steady streamwise vortices from the wake of wishbone and ramp VGs can explain the reason that their first two modes have the most turbulent kinetic energy.

4.3 Conclusion

The investigation of the mean velocity field demonstrated that the doublet VG has the largest wake region, which suggests a larger pressure drag. There was a small region of backward flow and a large deficit in the near wake of the doublet and ramp VGs. This has been associated with their larger VG wetted area compared to the wishbone VG. There were also two local minima in the wake of the double VG due to the interaction of flow with the two successive half-bodies of this geometry. The velocity deficit in the wake of the wishbone VG recovered faster than the other two VGs.

The largest mean wall-normal and spanwise velocity is observed in the wake of wishbone VG, suggesting more mixing between the freestream and the low-speed near wall flow. The doublet VG is shown to have the second largest wall-normal transport of flow while the ramp VG presents the smallest wall-normal motion. This has also been confirmed from the analysis of mean vorticity, such that the wishbone VG produces the strongest and the most coherent counter-rotating pair of streamwise vortices. The ramp VG has the weakest streamwise vortices with the smallest spanwise distance (i.e., narrower wake). The results also showed that the counter-rotating streamwise vortices are the dominant vortical pattern of the mean flow field for all the VGs. The pairs induce an upward flow at the centerline of the wake surrounded on both sides by regions of downward flow. The investigation of the coefficient of drag shows the ramp VG has the smallest device drag, followed by the wishbone and the doublet VG.

A narrow layer with high turbulence intensity is formed at the interface of the wake and free stream for all VGs. This layer thickens with increase of streamwise distance and has the largest intensity in the wake of the doublet VG. The double VG has the largest streamwise, wall-normal, and shear Reynolds stress, followed by the wishbone and the ramp VGs. The estimation of the turbulence production using the tomo-PIV data also indicates that the double VG generates the most turbulence kinetic energy.

The dominant coherent structure is determined to be a hairpin vortex instead of steady streamwise counter-rotating vortices in the instantaneous flow field. The POD analysis shows that the distribution of turbulent kinetic energy of the modes for the doublet VG is broader than the other two VGs. Therefore, the doublet VG produces more small-scale turbulence structures

compared to the other two VGs. The first POD mode for the wishbone and the ramp VGs contain a large amount of turbulent kinetic energy and is explained by the existence of a pair of relatively steady streamwise vortices. The visualization using Q-criterion also reveals that the hairpin vortices generated by the ramp VG are coherent in terms of both strength and shape. However, the hairpin vortices of the ramp are weaker than the ones generated by the other two VGs.

Overall, by comparing the wake of non-conventional VGs, we concluded that the wishbone VG with the least VG wetted area has the best performance in enhancing flow mixing. The doublet VG generated the highest level of turbulence and small-scale mixing, while it is expected to generate the largest pressure drag. Its second half body was the source of instability that increased turbulence production, and weakens the steady streamwise vortices.

Chapter 5. Vane-type VGs

5.1 Introduction

Vane-type VGs are the most common VGs in practical application due to their good performance in flow control and simple geometry. The first vane-type VGs were developed by Taylor (1947), and were speculated to forced flow mixing by transporting momentum form the free-stream to the near-wall region. The mixing mechanism was further studied by Schubauer and Spangenberg (1960) through their investigations of several VGs under adverse pressure gradient. They confirmed that the corresponding flow control mechanism is transfer of momentum between the high speed free-stream and the low-speed near wall flow. The investigations by Lin et al. (1990; 1999) also confirmed that, by generating streamwise vortices, vane-type VGs can accomplish a large transport of momentum. The rotating motion of the streamwise vortices ejects the low momentum flow away from the wall, and transfers the high momentum flow towards the wall. This provides sufficient kinetic energy to the boundary layer to relax the adverse pressure gradient and prevent/delay flow separation.

A disadvantage of large, conventional, vane-type VGs is the excessive mixing, which incurs a drag penalty. The streamwise vortices produced by conventional VGs dominate the flow field even after the flow has reattached (Lin, 1999). The parasitic drag of large conventional VGs was addressed by the application of low-profile VG (Kuethe, 1972). Various low-profile vane-type VGs were examined, and the comparison suggested that, in terms of delaying the separation and reducing reattachment distance, the vane-type VGs with $h/\delta \sim 0.2$ have perform similarly to vane-type VGs with $h/\delta \sim 0.8$. The visualization demonstrated that the generated streamwise vortices did not disturb the far downstream flow, proving that low-profile VGs provide enough flow mixing with lower drag.

The installation location of the VG and their vane arrangement were found to have effect on the flow control effectiveness. Previous literature revealed that a VG has the best performance when placed at the highest velocity point on an airfoil (Froster and White, 2014). The pairs of VGs with counter-rotating vortices are more effective in reducing the flow separation over high lift devices (Lin, 1999). Godard and Stanislas (2006) also concluded that the counter-rotating vortices are more effective.

The current study was conducted to investigate on the effect of the shape of the VG vane on the wake flow. State-of-the-art high-speed tomo-PIV system is applied to provide time-resolved three-dimensional measurement of the vortical structures and turbulence statistics in the near wake region. Three pairs of vanes with rectangular, delta, and trapezoidal shapes arranged in a symmetric configuration were placed in a laminar boundary layer. A single vane configuration was also investigated to characterize the interaction between vortices.

5.2 Results and Discussion

This section determines the effect of the vane shape on the wake flow of the VGs by comparing the mean flow, vorticity field, turbulence production, and dominant coherent structures from the instantaneous flow field. The subscript of a variable represents its direction, and $<>$ indicates the mean of the corresponding variable.

5.2.1 Wake flow with wall-normal velocities

The mean streamwise and wall-normal velocities are normalized with the free stream velocity U_∞, and their iso-surfaces are presented in Figure 5.1. The $0.9U_\infty$ iso-surfaces are rendered in transparent yellow to reveal the boundaries of the 3D wake. The blue iso-surface is the region of negative wall-normal velocity ($-0.1U_\infty$), and the green region represents the positive wall-normal velocity ($+0.1U_\infty$). Due to the limitation of the measurement volume in the wall-normal direction, the top of the iso-surfaces is cropped at $y=2.5h$. In Figure 5.1a, the cropping of the $0.9U_\infty$ iso-surface happens after $x = 6h$. The same cropping occurs at $x = 4h$ and $x = 3h$ for the TVG and the RVG in Fig 3b and 3c respectively. The observation reveals that the wake of the RVG has the fastest expansion in the wall-normal direction, followed by the TVG, and DVG. The expansion of the wake is associated with the lifting of the vortex core due to the self-induced upward velocity (Crow 2003). The $0.9U_\infty$ iso-surface shows that the DVG has the smallest wake region while the RVG has the largest wake region. The wake of the single RVG in Figure 5.1d expands slower in the wall-normal direction with respect to the RVG as seen by the location of the cropped iso-surface.

The iso-surfaces of wall-normal velocity indicate the extent of momentum transport between the free-stream and the near-wall region. In the wake of the DVG, two small blue iso-surfaces of downward motion can be observed along the sides of a larger upward motion along the wake centerline as shown by the green iso-surface. The TVG produces a stronger wall-normal velocity than the DVG, and the downward velocity iso-surfaces is present across the entire streamwise range. The RVG shows the largest upward and downward velocity iso-surfaces, as an indication of the strongest wall-normal flow mixing. In the wake of the single RVG, the upward and downward velocity iso-surfaces are equivalent in size. The difference between the pair and the single RVG demonstrates that the counter-rotating vortices intensify the transport of upward flow by inducing a focused motion.

The streamwise vortex is expected to be between the iso-surfaces of positive and negative wall-normal velocity. The results also show that the gap between the vortex cores tends to be smaller as the sweep angle of the vane leading-edge becomes larger. The RVG has the largest distance between the counter-rotating vortices while its vane has zero sweep. On the other hand, the DVG has the smallest distance between the vortices and the largest vane sweep angle. The vortex in the wake of the single RVG is observed to be inclined and gradually move away from the trailing-edge of the VG.

The larger sweep angle of the vane also results in smaller frontal area of the VG and leads to a smaller wake region. However, as it was observed in Fig 3, the momentum transport by wall-normal motions reduces as the leading-edge sweep angle increases.
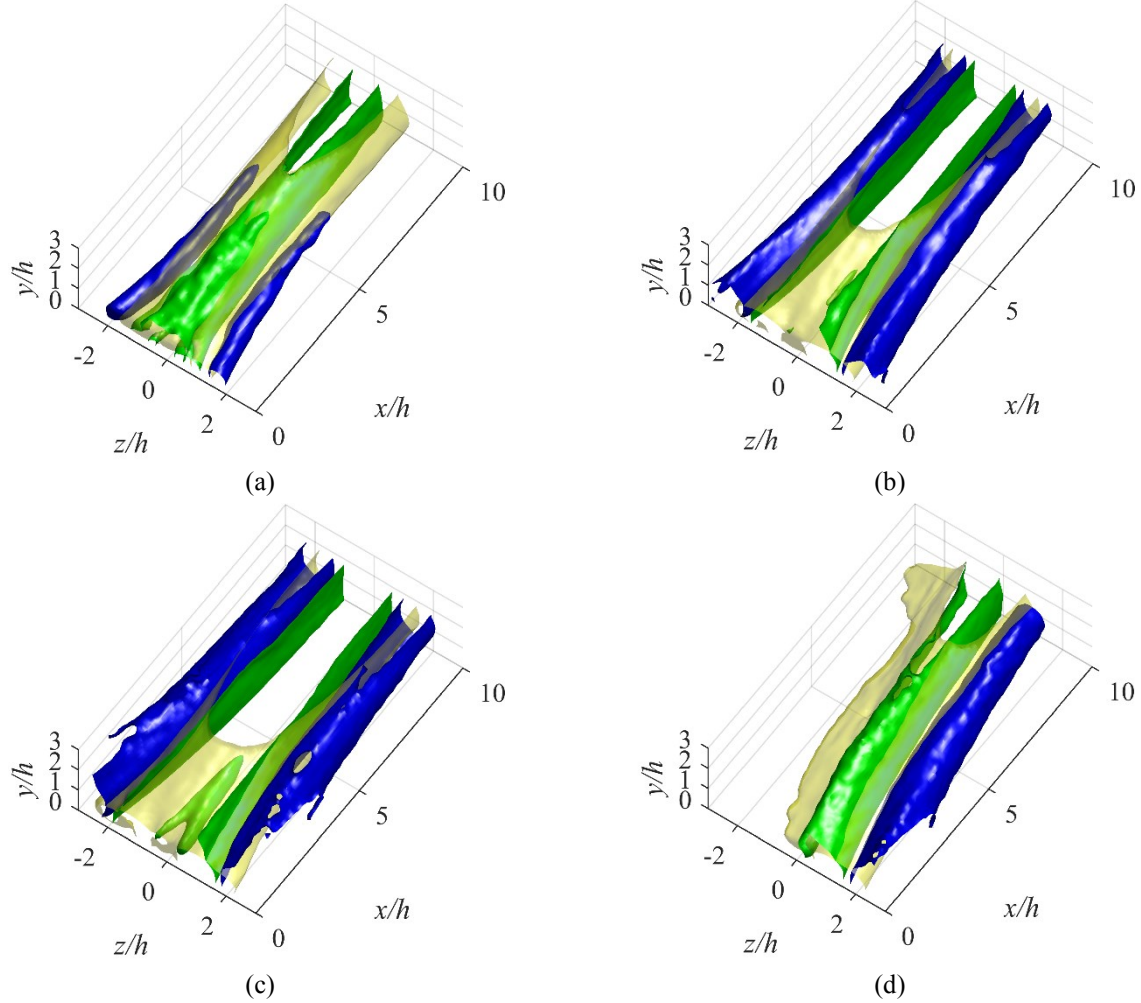
Figure 5.1. Mean velocity iso-surfaces in the wake of a pair of (a) the DVG, (b) the TVG, (c) the RVG, and (d) the single RVG. The transparent yellow iso-surface shows mean streamwise velocity at $<U> = 0.9U_\infty$. The green and blue iso-surfaces show mean wall-normal velocity at $<V> = +0.1U_\infty$ and $-0.1U_\infty$, respectively.

5.2.2 Velocity recovery

The recovery of wake deficit is shown by plotting the mean streamwise velocity at three different levels in Figure 5.2. Transparent yellow, transparent green and solid blue are used to indicate iso-surfaces of $0.7U_\infty$, $0.6U_\infty$, $0.5U_\infty$, respectively. As seen in Figure 5.2a, the DVG has the fastest velocity recovery. The $0.5U_\infty$ iso-surfaces last till $x \approx 4h$, and the $0.6U_\infty$ iso-surfaces last till $x \approx 6h$. In the wake of the TVG, the $0.5U_\infty$ iso-surfaces last much longer, such that they can still be observed at $x = 8h$. Also, the $0.6U_\infty$ iso-surfaces are detected through the entire measured streamwise range. The RVG also present a weaker velocity recovery compared to the DVG. The $0.5U_\infty$ iso-surfaces are first observed at the vortex core locations of the primary and secondary vortices at $x = 0$. The $0.5U_\infty$ region from the primary vortices lasts till $x \approx 4h$, while the $0.5U_\infty$

59

region from the secondary vortices only lasts about $1h$ in streamwise direction. The $0.6U_\infty$ iso-surfaces are detected from $x = 0$ to $x = 10h$.

It suggests that the DVG recovers the fastest due to its initial smaller wake deficit. The TVG, however, shows a slower recovery than the RVG, due to its less efficient wall-normal flow mixing. The contour of Figure 5.2d also suggests that the single RVG has a higher recovery rate with respect to the RVG. It indicates that the presence of the counter-rotating vortex pair slows down the velocity recovery.
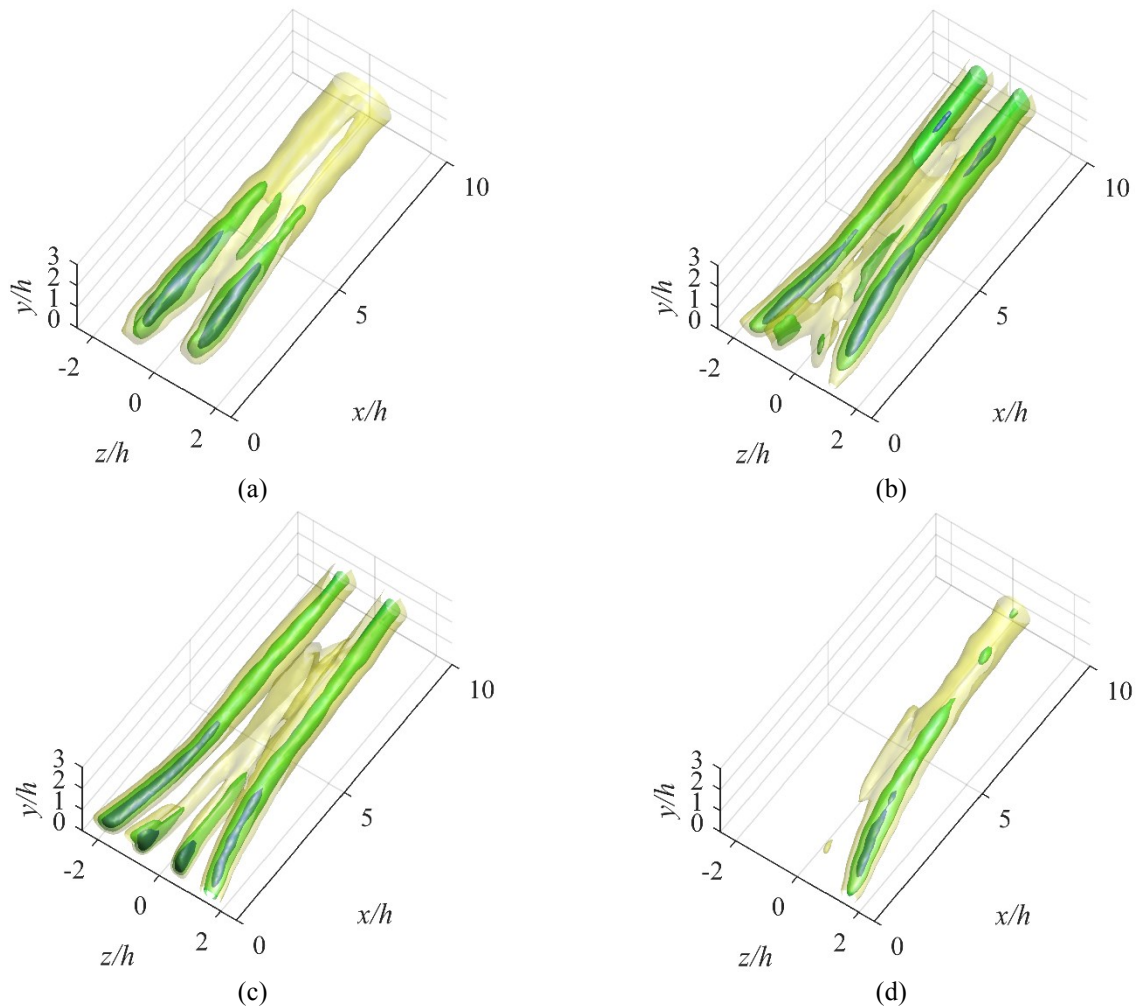
Figure 5.2. Iso-surfaces of mean streamwise velocity in the wake of (a) the DVG, (b) the TVG, (c) the RVG, and (d) the single RVG. The iso-surface colored with transparent yellow, transparent green, and solid blue represent mean streamwise velocity $<U> = 0.7U_\infty$, $<U> = 0.6U_\infty$, and $<U> = 0.5U_\infty$, respectively.

5.2.3 Coefficient of drag

The values of C_D of vane-type VGs are calculated using Equation (4.3), and are shown in Table 5.1 with information of wetted area and frontal area. The result shows that the single RVG, indicated by RVG(s) in Table 5.1, has the lowest C_D magnitude. The RVG shows the largest drag, followed by the TVG and the DVG. This agrees with the observation from Figure 5.1. The device drag is correlated with the size of the wake region.

Table 5.1. C_D for different vane-type VGs at $x = 5h$

VG	VG Wetted Area(mm^2)	Total Wetted Area(mm^2)	Frontal Area(mm^2)	C_D
DVG	620	2037	116	0.0106
TVG	850	2267	168	0.0142
RVG	1110	2527	220	0.0184
RVG(S)	555	2118	110	0.0097

5.2.4 Mean vorticity

The iso-surfaces of mean streamwise vorticity, $<\Omega_x>$, normalized with U_∞/h, are plotted in Figure 5.3. The negative vorticity is rendered in yellow with a threshold of -0.02, and the positive vorticity is shown in red with a threshold of +0.02. The thresholds were selected to visualize both the primary and secondary vortex structures. The mean vorticity was obtained by calculating the velocity gradient using the second order central difference theorem. In the wake of all VG pairs, counter-rotating primary vortices are formed. The vortex tubes converge toward each other at the immediate downstream of the VG trailing-edge and become parallel after $x \approx 2h$. A pair of weaker secondary counter-rotating vortices are also detected between the primary vortices. The secondary vortex pair rotates in the opposite direction to the primary vortex pair. At the selected threshold, the iso-surfaces of the secondary vortices only exist until $x \approx 3.5h$, while the iso-surfaces of the primary vortices can be clearly observed through the entire measurement domain. The vortices generated by the TVG and RVG are stronger than the DVG. In comparing Fig 5c and 5d, we conclude that the VG pair configuration slightly increases the vortex strength of both the primary and secondary vortices, especially at the near wake region. The $<\Omega_x>$ analysis suggests that the RVG produces the strongest streamwise vortices, followed by the TVG and the DVG.

61
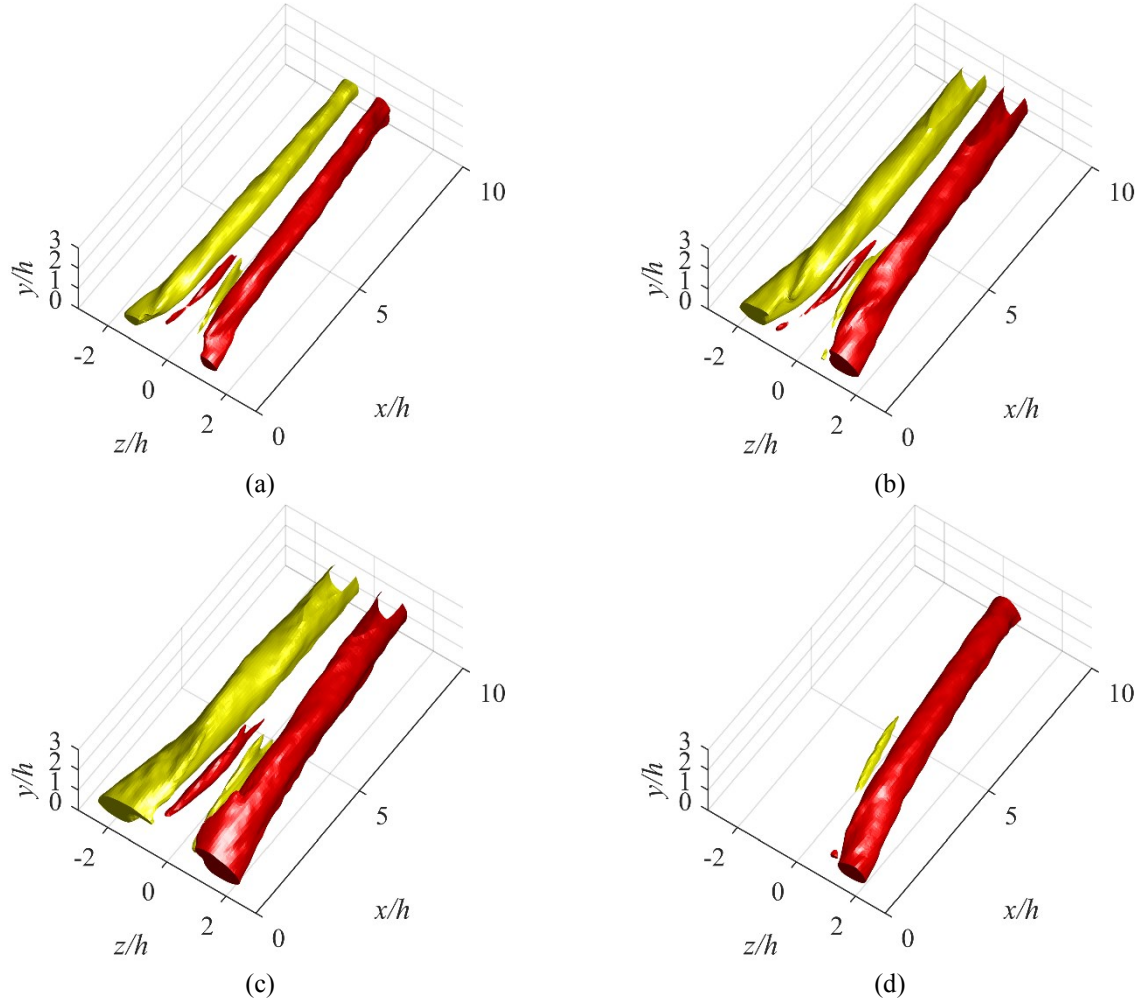
Figure 5.3. A visualization of the mean streamwise vorticity, $<\Omega_x>$, normalized by U_∞/h in the wake of (a) the DVG, (b) TVG, (c) RVG, and (d) the single RVG. The positive $<\Omega_x>$ (clockwise) is colored in red with a threshold of +0.02, while the negative $<\Omega_x>$ is presented in yellow at a threshold of -0.02. Primary and secondary streamwise vortices are observed in all the wakes. As the sweep angle of the vane leading-edge reduces, the steady vortices tend to be stronger.

5.2.5 Vorticity fluctuation

The mean of the square of vorticity fluctuation, $<\omega_x^2>$, normalized with U_∞^2/h^2, is presented in Figure 5.4 with a threshold of 3.5, to show the level of turbulent kinetic energy in the wake of VGs. A regression with a kernel of two pixels was applied to the velocity field in order to reduce the noise level of the vorticity field. The contour of the DVG from Figure 5.4a shows that the vortices at the immediate downstream of the trailing-edge do not contain a significant amount of vorticity fluctuation. At $x = \approx2.5h$, the two iso-surfaces become closer and merge at the selected threshold. This merged region of high vorticity fluctuation also overlaps with the location of the secondary vortices observed in Figure 5.4. The TVG and RVG also have a similar pattern, and a

strong vorticity fluctuation can be observed at the immediate downstream of the trailing-edge of the VGs. In general, the largest vorticity fluctuation is generated by the RVG and the weakest by the DVG.

Figure 5.4d shows that the single RVG produces a tube of vorticity fluctuation with a relatively large diameter, which is inclined at an angle with respect to the flow direction. The corresponding iso-surface at the downstream of its trailing-edge shows a shape similar to the iso-surface observed from the wake of the RVG. However, the iso-surface maintains its diameter as the streamwise distance increases. This suggests that the reduction of streamwise vorticity fluctuations is associated with the stabilizing effect of the neighboring counter-rotating vortices after $x/h \approx 5$ in the wake of the VG pairs.
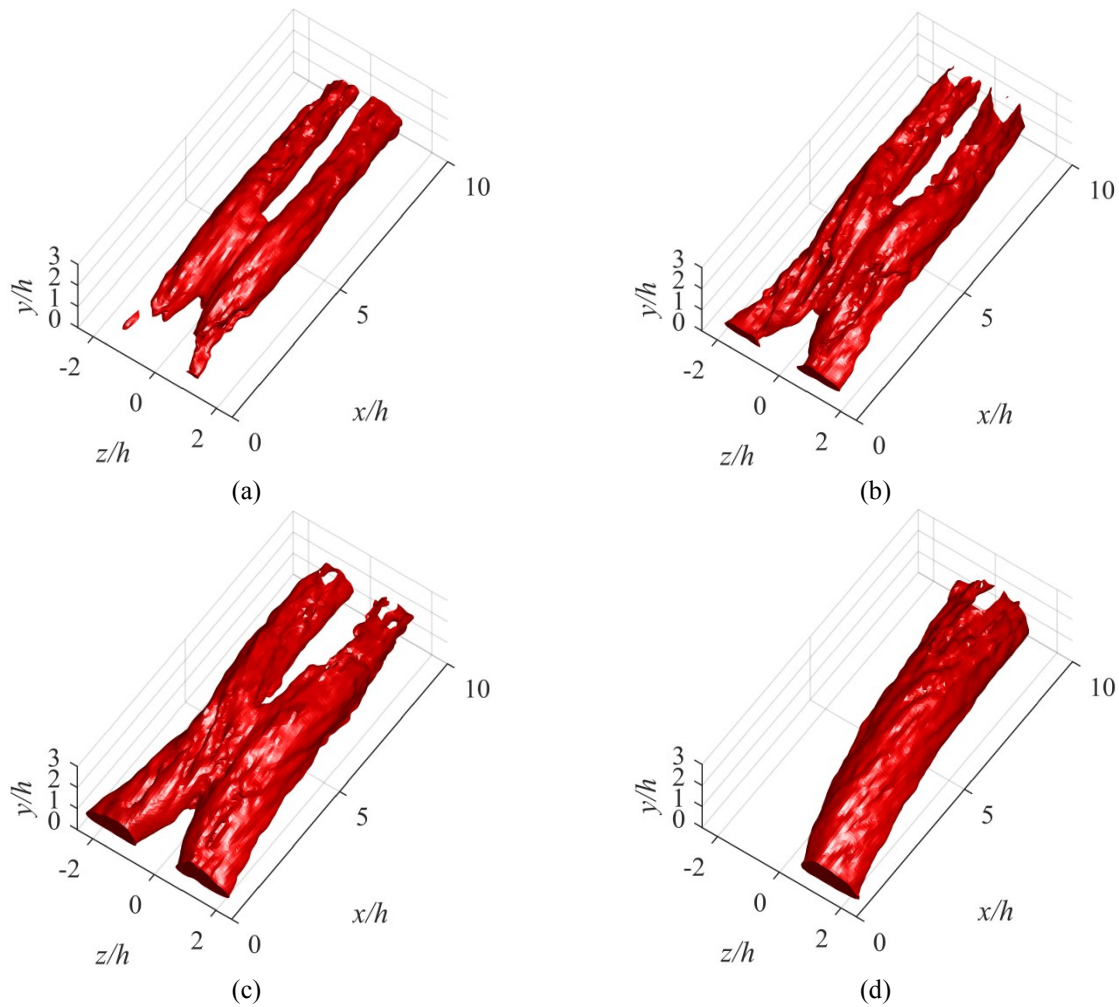
Figure 5.4. The time-average of square of the streamwise vorticity fluctuation, $<\omega_x^2>$, normalized with U_∞^2/h^2 in the wake of (a) the DVG, (b) the TVG, (c) the RVG, and (d) the single RVG. The proximity of the pairs of counter-rotating vortices has a stabilizing effect and reduces the vorticity fluctuation.

5.2.6 Turbulence production

The production of turbulence kinetic energy is investigated to compare the ability of extracting energy from the mean flow for different VGs. This energy extracting process is expected to increase the small-scale mixing, and therefore improve the flow mixing. The production of turbulence, $<P>$, is demonstrated in Equation (4.4).

The contour of the turbulence production $<P>$ is normalized using $U_\infty^3 h$, and is presented in Figure 5.5. The intensity variation of the $<P>/(U_\infty^3 h)$ is represented using three different color iso-surfaces. The solid red iso-surface represents the production region with the highest intensity, which has a threshold of 0.05. The solid orange iso-surface has a threshold of 0.02, and the transparent yellow iso-surface has a threshold of 0.01. The contour of DVG in Fig 7a shows that the strongest region of turbulence production lies within x=0-2h, near the trailing-edge of the VG. As the streamwise distance increases, the magnitude drops rapidly. The transparent iso-surface stays thick, and stays visible till $x = 6h$. A similar contour pattern is also observed in the wake of the TVG, except the contour is less visible. In the wake of the RVG, the production contour is not as strong as in the wake of the DVG. It is wider than the DVG and the TVG, and lies along the primary and secondary vortex cores observed in Figure 5.2c. The contour of production in Figure 5.5d reveals that the single streamwise vortex can extract more kinetic energy from the mean flow than the RVG. The whole streamwise vortex is surrounded by the transparent yellow iso-surface, with two strong production regions shown close to trailing-edge region. The difference in pattern between the contours of the pair and single RVG indicates that the conjugate vane-blade has a significant effect in reducing turbulence production within the close wake region.
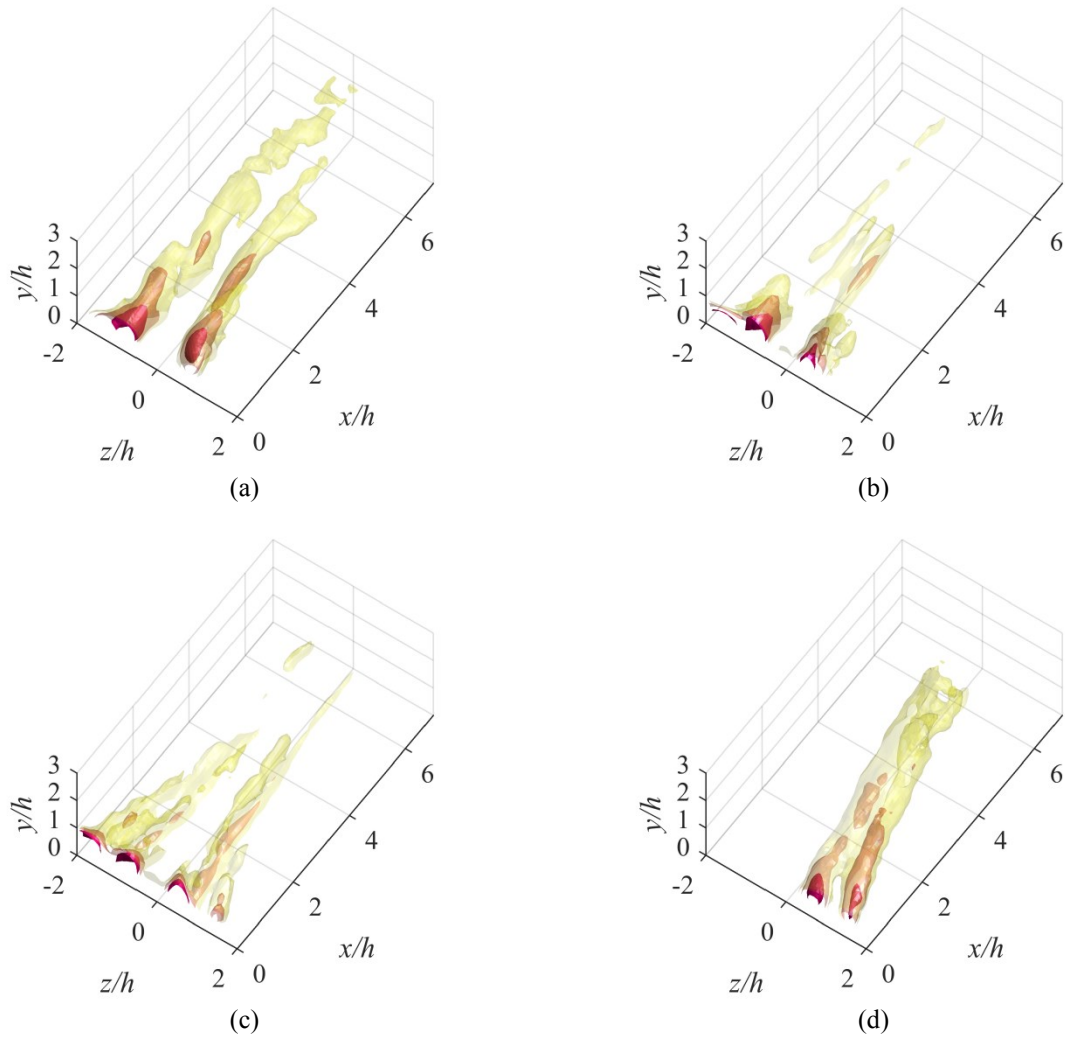
Figure 5.5. Iso-surfaces of normalized turbulence production $<P>/(U_\infty^3 h)$ in the wake of (a) the DVG, (b) the TVG, (c) the RVG, and (d) the single RVG. Three levels of thresholds are selected to represent the intensity variation. The red iso-surfaces have a threshold of 0.05, and the orange, transparent yellow iso-surfaces have thresholds 0.02, and 0.01 respectively. For the VGs in pair, DVG has the most turbulence production.

5.2.7 Proper-orthogonal-decomposition analysis

The three-dimensional coherent structures are investigated through proper-orthogonal-decomposition (POD), using the snapshot method (Lumley, 1967; Sirovich, 1987). The time-resolved fluctuating field was used in the POD analysis to identify the dominant structures and reconstruct a low-order model. As seen in Figure 5.6a, the RVG has a large percentage of energy (≈23%) in the first POD mode. The energy of the first mode of the single RVG, however, has only 8%. The energy of the first POD mode for the other two VGs is much smaller compared to the rectangular vane group. It is concluded that the mode energy distribution tend to be flat when

65

the leading-edge sweep angle is large. The cumulative mode energy distribution is presented in Figure 5.6b. It is observed that the VGs in pairs have a similar growing trend, while the single RVG shows a faster growing.
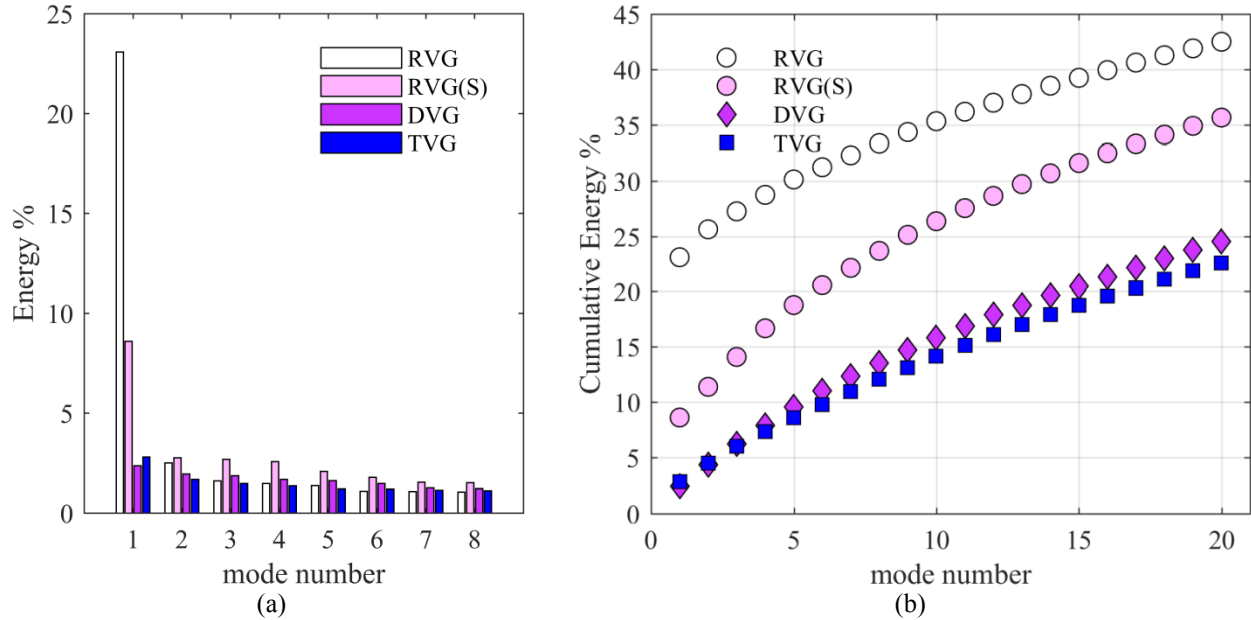
Figure 5.6. (a) Distribution of POD mode energy and (b) cumulative mode energy distribution for all VGs based on the fluctuating flow field of 3,300 tomo-PIV images.

The first POD mode has the highest level of turbulent kinetic energy from the fluctuating velocity field, which indicates that it has the most impact on the whole velocity field. To study the difference of the first POD mode of each VG, the vortex structures of the first POD mode are illustrated in Figure 5.7 using Q-criterion (Hunt 1998). The iso-surfaces are constructed with a threshold of 0.5 s^{-1}. The result of Figure 5.7 shows that the rank of the number of small-scale vortices is inversely proportional to the rank of percentage energy of the first mode. As shown in Figure 5.7c, the first mode of the RVG only contains two small streamwise vortices which follow the pattern of the primary vortices from the mean flow field. In the case of the single RVG from Figure 5.7d, it also has two streamwise vortices along the region where the primary streamwise vortex lays. However, as seen in Figure 5.7a and b, the vortex pattern in the wake of DVG and the TVG are more random compared to the rectangular VG group. More small-scale vortices are observed. It is believed that those small-scale vortices are responsible for weakening the primary streamwise vortices.
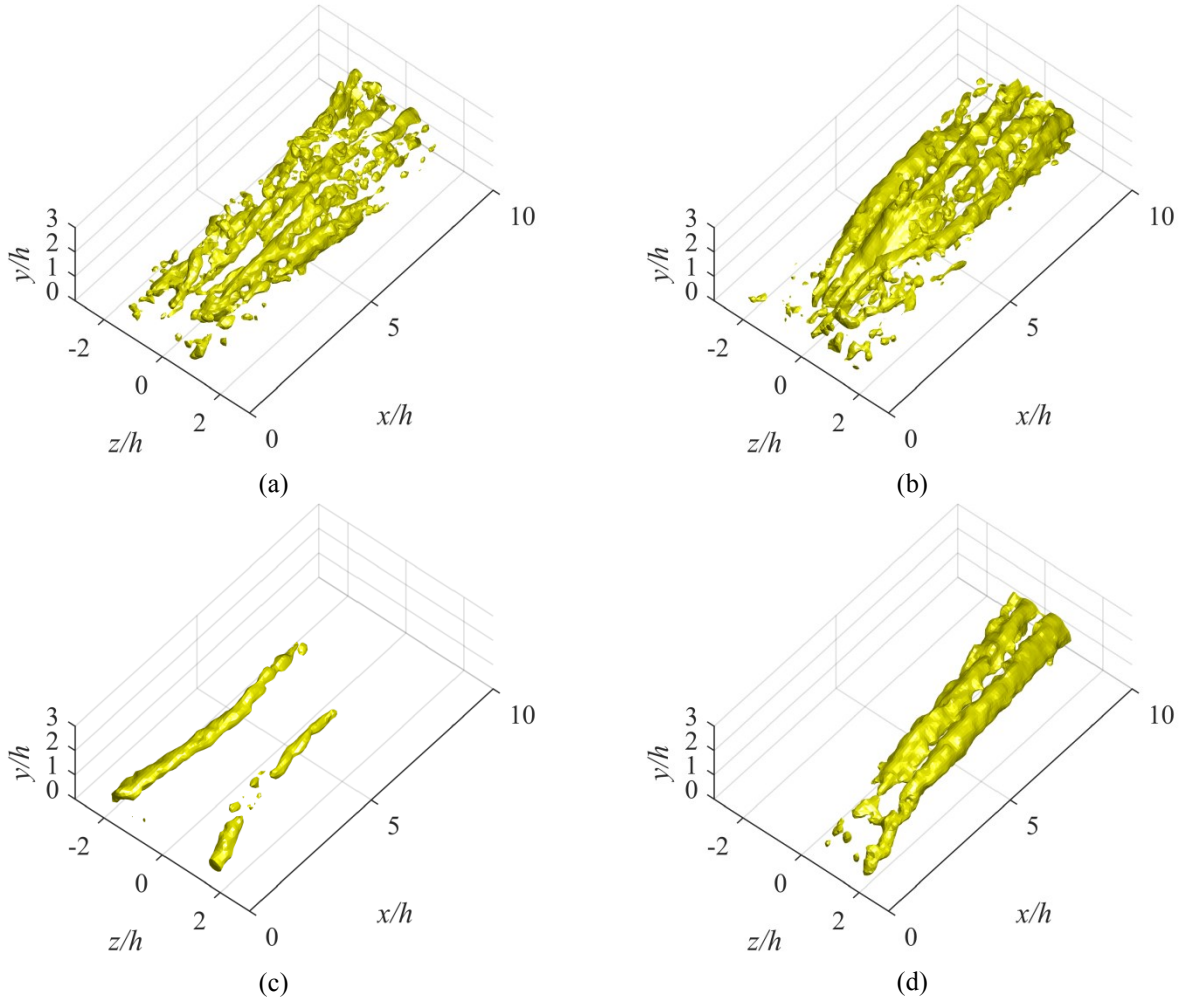
Figure 5.7. Visualization of the coherent vortex structures from the first POD mode using a threshold of 0.5 s^{-1} for (a) the DVG, (b) the TVG, (c) the RVG, and (d) the single RVG.

5.2.8 Coherent structures

To visualize the instantaneous turbulent coherent structures within the wake region, we reconstructed the flow field using the mean flow field and 40% of the total energy from fluctuating flow field. The energy level was selected to eliminate the small-scale turbulence with minimum change to the dominant turbulent structures. The reconstruction for the DVG and TVG requires 48 and 56 modes, respectively. In contrast, the RVG and the single RVG use 16 and 26 modes, respectively.

The dominant vortex structures from the wakes of different VGs are presented in Figure 5.8 using Q-criterion. The instantaneous wall-normal velocities are also presented to illustrate the transport of momentum and direction of rotation of the vortices. The Q-criterion iso-surfaces are

rendered in solid yellow with a threshold of 80 s^{-2}. The positive instantaneous wall-normal velocity is colored using transparent green, and the negative instantaneous wall-normal velocity is shown in transparent blue. The thresholds for positive and negative wall-normal velocities have magnitudes of 0.04 and 0.02 respectively. The primary turbulent structure is observed to be a pair of streamwise counter-rotating vortices near the wall for all VGs. The difference in thresholds also suggests that, the upward flow motion is stronger than the downward flow motion.

As seen in Figure 5.8a, the DVG produces a large number of secondary vortices near the wake centerline. A better view is presented in the animation (Supp_Video_S4.avi); numerous small-scale vortices are observed around the primary vortices even when the flow field is reconstructed using only 40% of the turbulent kinetic energy from the unsteady velocity field. The small-scale spanwise transverse vortices have a tendency to arch over the wake centerline. However, due to the limitation of the measurement volume in the y-direction, the transverse hairpin-like tip cannot be clearly detected. The primary vortices are also weaker compared to the RVGs; this can be explained by the discussion of the first POD mode above. The small-scale turbulent structures weaken the primary vortices through vorticity cancellation. The iso-surfaces of the wall-normal velocities indicate that the wall-normal flow transport is also weaker compared to the other VGs.

The reconstructed model of the instantaneous wake of the TVG is presented in Figure 5.8b. Wall-normal transverse vortices can be observed from the animation (Supp_Video_S5.avi) between the counter-rotating streamwise vortices. The number of small-scale structures is much lower than in the DVG, and the primary streamwise vortices are also weaker than the RVGs, but stronger than the DVG.

The wake of the RVG is illustrated in Figure 5.8c. The secondary vortex takes form of wall-normal transverse vortex, inclined to fit the velocity profile. The animation (Supp_Video_S6.avi) demonstrates that the secondary vortices stay visible till $x = \approx 5h$. The RVG produces the most coherent, and the strongest primary vortices compared to the DVG and the TVG.

As shown in Figure 5.8d, the secondary vortices in the wake of the single RVG are U shape spanwise transverse vortices; they are observed after $x = 6h$. The animation (Supp_Video_S7.avi) shows that the secondary vortices are formed as wall-normal transverse

vortices first. As they move downstream, they tend to grow in spanwise direction, and connect to the primary vortex, form a U shape. The contour of the wall-normal velocities also suggests that the upward flow transport is stronger than the downward transport. The difference between the contours of the RVG and the single RVG reveals that the counter-rotating pair configuration can significantly weaken the secondary vortices.
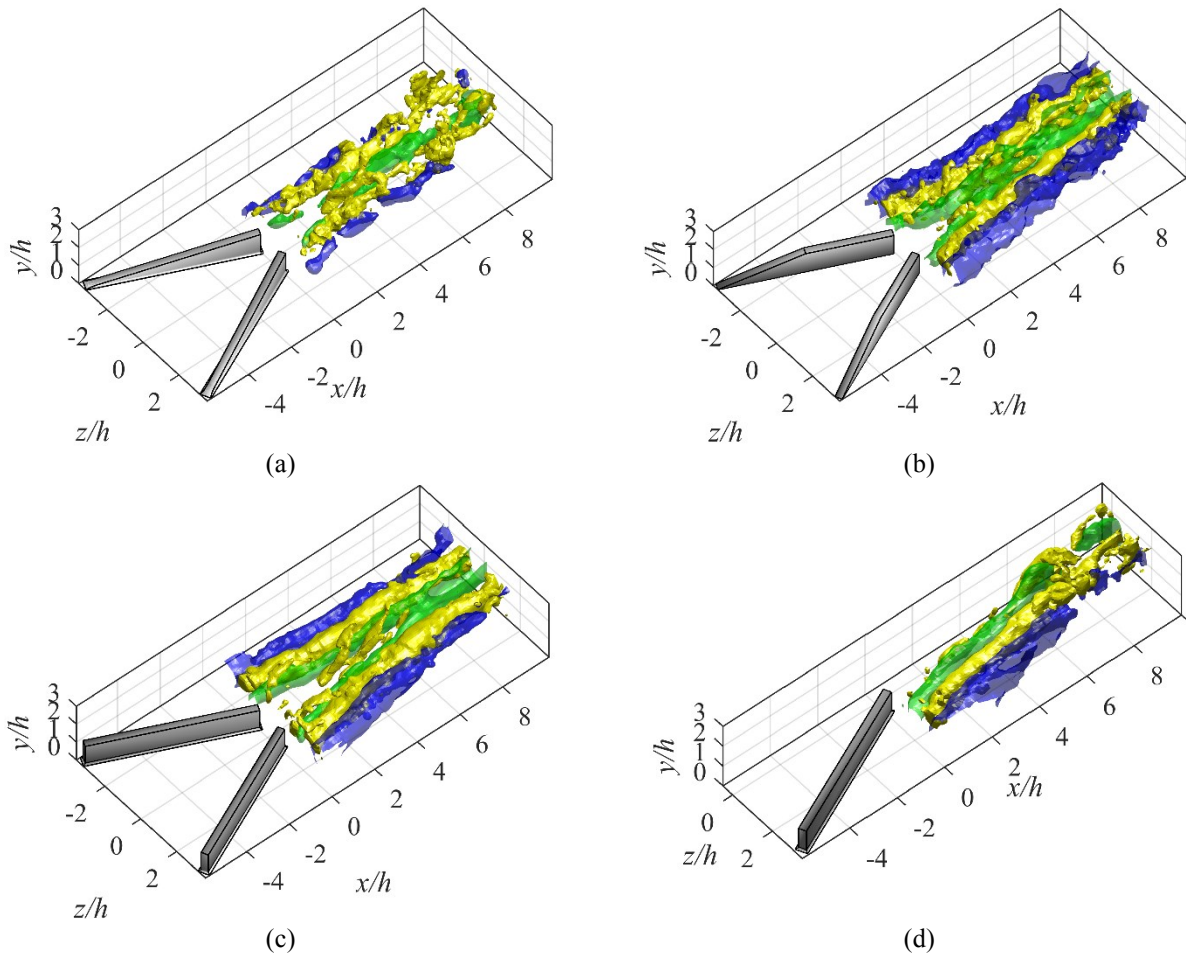
Figure 5.8. Low-order reconstruction of instantaneous coherent structures using the mean flow and 40% of total turbulence kinetic energy from the fluctuating flow. *Q*-criterion (solid yellow), and wall-normal velocities (green: $V > 0$; blue: $V < 0$) for a) the DVG, b) the TVG, c) the RVG, and d) the single RVG. The thresholds for the *Q*-criterion, positive, and negative wall-normal velocities are 80 s^{-2}, 0.04 m/s, and -0.02 m/s respectively.

5.3 Conclusion

Overall, the RVG presents the strongest wall-normal motion, which suggests that it is the most effective VG for improving the wall-normal momentum transfer process. The second-best VG is the TVG. The VGs mentioned above produce a pair of consistently strong counter-rotating vortices, which is the key element in enhancing the flow mixing. In contrast, the DVG produces much weaker streamwise vortices, which has limited effect in improving the wall-normal flow exchange. It suggests that increasing the leading-edge sweep angle will lower the strength of the primary vortices, and therefore reducing the wall-normal flow transport. As the vane body tends to be more "swept," the distance between the two primary streamwise vortices will be reduced. As a result, the turbulence level from the interaction region is strengthened. This extra turbulence interferes with the primary vortices produced by the VGs and weakens their coherency and strength. In terms of the device drag, the RVGs have much higher drag than the VGs with swept leading-edge. The result of the coefficient of drag study tells that the RVG has the largest parasitic drag, followed by the TVG, the DVG, and the single RVG. The comparison between the RVG and the single RVG also shows that the VG in counter-rotating pair produces a wake with lower turbulence level, which has fewer disturbances to the primary vortex structures. The study suggests the counter-rotating vane configuration could reduce the device drag by stabilizing the primary vortices. Increasing the sweep angle of the leading-edge can largely decrease the device drag to a certain extent. However, increasing the angle further has limited effect. This indicates that an optimal leading-edge angle exists, which can significantly reduce the drag while still produce effective flow mixing.

Chapter 6.   Conclusion

The investigation of the mean flow fields of non-conventional VGs suggests that the doublet VG has the largest wake region, followed by the wishbone VG. The velocity recovery result from the mean streamwise contours reflects that the doublet and the ramp VG decelerate the flow more than the wishbone VG due to their larger VG wetted area. The velocity deficit profile also suggests that the wishbone VG has the fastest velocity recovery within the near wake region ($x =$ 0-10h). The local minimum velocity in the wake of wishbone VG recovers to approximate $0.4U_\infty$ at $2h$ downstream of the trailing-edge, while the other two VGs only reach $\approx 0.2U_\infty$ velocity recovery at the same downstream location. In terms of the wall-normal fluid transport, the wishbone VG has the most significant effect in enhancing the flow exchanging between the low-speed region and free-stream. The doublet VG is shown to be the second efficient device. The ramp VG presents negligible wall-normal motion compared to the other two VGs. This has also been confirmed from the vorticity analysis, such that the wishbone VG produces the strongest counter-rotating streamwise vortices with the least core vorticity decay. The doublet VG generates the second strongest streamwise vortices. The contour also reveals that the counter-rotating streamwise vortices are the dominant vortex structures in the mean flow field for all the VGs. The turbulence production result proves that the doublet VG can extract the most kinetic energy from the mean flow. The ramp VG is the weakest in this case. This matches the result from the Reynolds stress analysis, which states that the doublet VG has the highest level of turbulence in the near wake region.

When considering the instantaneous flow field of non-conventional VGs, the dominant coherent structure is concluded to be hairpin vortex instead of steady streamwise counter-rotating vortices. The POD analysis shows that the mode energy distribution for the doublet VG is broader than the other two VGs. It suggests that the doublet VG produces more small-scale turbulence structures compared to the other two VGs. This result matches the turbulence production result, and is proved by the Q-criterion vortex visualization. The first two POD mode for the wishbone and the ramp VG contain the most energy is being explained by the existence of a pair of relatively strong streamwise vortices. The Q-criterion visualization also reveals that the hairpin vortices generated by the ramp VG show a good consistency in terms of both strength and shape.

However, these hairpin vortices are still much weaker than the ones generated by the other two VGs. Hence they are not effective in flow control purpose.

By comparing the wake of non-conventional VGs, the wishbone VG with the least VG wetted area is concluded to have the best performance in enhancing flow mixing. The doublet VG with double row of wedge geometry shows the highest level of turbulence. Its second half body can be the resource of the instability that induces the most turbulence production, and weakens the steady streamwise vortices. The ramp VG is shown to have the least effect in improving flow exchange.

The analysis of the mean flow fields of the vane-type VGs reveals that the RVG has the strongest wall-normal motion, which suggests that it is the most effective VG for improving the wall-normal momentum transfer process. The second-best VG is the TVG. The VGs mentioned above produce a pair of consistently strong counter-rotating vortices, which is the key element in enhancing the flow mixing. In contrast, the DVG produces much weaker streamwise vortices, which has limited effect in improving the wall-normal flow exchange. It suggests that increasing the leading-edge sweep angle will lower the strength of the primary vortices, and therefore reducing the wall-normal flow transport. The shape of vane-blade shows significant on the vortex pattern. The distance between the two primary streamwise vortices will be reduced when the leading edge of the vane-blade is more swept. As a result, the turbulence level from the interaction region is strengthened. This extra turbulence interferes with the primary vortices produced by the VGs and weakens their coherency and strength. In terms of the device drag, the RVGs have much higher drag than the VGs with swept leading-edge. The investigation of the coefficient of drag suggests that the RVG has the largest parasitic drag, followed the TVG, the DVG, and by the single RVG. The comparison between the RVG and the single RVG demonstrates that the VG in counter-rotating pair produces a wake with lower turbulence level, which has fewer disturbances to the primary vortex structures.

The instantaneous visualization of the wake of the vane-type VGs shows that the dominant primary vortex is a pair of counter-rotating streamwise vortices. The secondary vortices in the wake of the RVG and TVG are wall-normal transverse vortices, inclined to fit the velocity profile. In the wake of the DVG, the secondary vortices tend to arch over the wake and form hairpin-tip like shape. In the single RVG case, the secondary vortex first appeared as wall-

normal transverse vortices, and later attached to the primary streamwise vortex to form a transverse vortex arc. The investigation of the instantaneous coherent structure indicates that the coherency and strength of the generated vortex structure is inversely proportional to the sweep angle of the vane leading-edge. Associating with the proper-orthogonal-decomposition analysis, the mode energy distribution becomes flatter as the leading-edge sweep angle increases. The DVG, with the largest sweep angle, produces more small-scale turbulence than the other VGs, which reduced the coherency of the primary vortices and the momentum transportation toward the wall.

The study suggests the counter-rotating vane configuration could reduce the device drag by stabilizing the primary vortices. Increasing the sweep angle of the leading-edge can largely decrease the device drag to a certain extent. However, increasing the angle further has limited effect. This indicates that an optimal leading-edge angle exists, which can significantly reduce the drag while still produce effective flow mixing.

In conclusion, vane-type VGs tend to have larger wake region, as well as larger device drag, compared to non-conventional VGs. This is largely due to the gap between the vanes. The gap allows some flow to pass through and separate the two streamwise vortices from each other. It significantly reduces the mutual damping effect from two counter-rotating vortices; thus, enhancing the individual streamwise vortex strength. Therefore, the primary streamwise vortices in the wake of vane-type VGs are generally stronger than the ones generated by the non-conventional VGs. Based from observation from the mean flow field, the primary vortices generated by the vane-type VGs persist longer in streamwise distance when compared to the ones generated by the non-conventional VGs. In addition, strong primary vortices in the wake of the vane-type VGs produced secondary streamwise vortices, an observation unique to this type of VG. When considering the instantaneous flow field, it is noticeable that non-conventional VGs tend to generate more obvious hairpin vortices. The sudden stall at the joint center of the non-conventional VGs is believed to be responsible for the shedding of transverse hairpin head.

A strong shear region is created as the flow climb over the obstacle. On the other hand, the transverse vortices from the wake of the vane-type VGs have a higher likelihood to be generated by the strong shear layer induced by the wake and free stream. The analysis showed that the effective wall-normal mixing distance is a significant factor in selecting VG, when considering the device drag and flow control effectiveness.

Bibliography

Acalar, M. S., & Smith, C. R. (1987). A study of hairpin vortices in a laminar boundary layer. Part 1. Hairpin vortices generated by a hemisphere protuberance. *Journal of Fluid Mechanics*, 1-41.

Altenhofen, R. E. (1952). Rectification. In *Manual of Photogrammetry* (p. 457). Washington: American Societry of Photogrammetry.

Arroyo, M. P., & Greated, C. A. (1991). Stereoscopic particle image velocimetry. *Meas Sci Technol*, 1181-1186.

Ashjaee, J., & Johnston, J. P. (1980). Straight-waller, two-dimensional diffusers - Transitory stall and peak pressure recovery. *Journal of Fluids Engineering*, 275.

Barrett, R., & Farokhi, S. (1993). On the aerodynamics and performance of active vortex generators. *11th Applied Aerodynamics Conference*, (pp. 376-386). Reston.

Basset, A. B. (1888). *Treatise on Hydrodynamics vol II*. London, Deighton: Bell & Co.

Baur, X., & Kongeter, J. (1999). PIV with high temporal resolution for the determination of local pressure reductions from coherent turbulent phenomena. *3rd Int Symp PIV*. Santa Barbara.

Betterton, J. G., Hackett, K. C., Ashill, P. R., Wilson, M. J., Woodcock, I. J., Tilman, C. P., & Langan, K. J. (2000). Laser doppler anemometry investigation on sub boundary layer vortex generators for flow control. *Tenth International Symposium on Applications of Laser Techniques to Fluid Mechanics* , (pp. 10-13).

Betterton, J., Hackett, K., Ashill, P., Wilson, M., & Woodcock, I. (2000). Laser doppler anemometry investigation on sub boundary layer vortex generators for flow control. *10th International Symposium on Applications of Laser Techniques to Fluid Mechanics*, (pp. 10-13).

Bohl, D. G., & Koochesfahani, M. M. (2009). MTV measurements of the vortical field in the wake of an airfoil oscillating at high reduced frequency. *J Fluid Mech*, 63-88.

Calluaud, D., & David, L. (2004). Stereoscopic particle image velocimetry measurements of a flow around a surface-mounted block. *Exp. Fluids*, 33-61.

Carmichael, B. H. (1981). *Low Reynolds number airfoil survey*. NASA.

Coles, D. (1956). The law of the wake in the turbulent boundary layer. *J Fluid Mech*, 191-226.

Coles, D., & Hirst, E. (1969). Computation of turbulent boundary layers; 1968 AFOSR-IFP-Stanford Conference. *Conference on Computation of Turbulent Boundary Layers.*

Coudert, S., & Schon, J. P. (2001). Back-projection algorithm with mis-alignment corrections for 2D3C stereoscopic PIV. *Meas Sci Technol,* 1371-1381.

Crow, S. C. (2000). Stability theories for a pair of trailing vortices. *AIAA,* 293-300.

Elsinga, G. E., Scarano, F., Wieneke, B., & van Oudheusden, B. W. (2005a). Tomographic particle image velocimetry. *6th Int Symp PIV.* Prasadena.

Elsinga, G. E., Scarano, F., Wieneke, B., & van Oudheusden, B. W. (2005b). Assessment of tomo-PIV for three-dimensional flows. *6th Int Symp PIV.* Prasadena.

Elsinga, G. E., Scarano, F., Wieneke, B., & van Oudheusden, B. W. (2006). Tomographic particle image velocimetry. *Exp Fluids,* 933-947.

Elsinga, G. E., Westerweel, J., Scarano, F., & Novara, M. (2010). On the velocity of ghost particles and the bias errors in tomographic -PIV. *Exp Fluids,* 825-838.

Froster, K. J., & White, T. R. (2014). Numerical investigation into vortex generators on heavily cambered wings. *AIAA,* 1059-1071.

Gauthier, V., & Riethmuller, M. L. (1988). Application of PIDV to complex flows: measurements of the thirs component. . *VKI Lecture Series on Particle Image Displacement Velocimetry.*

Ghosh, S., Choi, J., & Edwards, J. R. (2010). Numerical simulations of effects of micro vortex generators using immersed-boundary methods. *AIAA,* 92-103.

Godard, G., & Stanislas, M. (2006). Control of a decelerating boundary layer. Part 1: Optimization of passive vortex generators. *Aerospace Science and Technology,* 181-191.

Herman, G. T., & Lent, A. (1976). Iterative reconstruction algorithms . *Comput Biol Med,* 273-294.

Hunt, J. C., Wray, A. A., & Moin, P. (1998). *Eddied, stream, and convergence zones in turbulent flows.*

Janiszewska, J., Gregorek, G., & Lee, J. (2004). The LS(1)-0417MOD Airfoil Aerodynamics Flow Characteristics with the Application of Vortex Generators. *42nd AIAA Aerospace Sciences Meeting and Exhibit,* (pp. 1-10).

Kim, S. K., & Chung, S. K. (2004). An investigation on airflow in disordered nasal cavity and its corrected models by tomographic PIV. *Meas Sci Technol,* 1090.

Kolář, V. (2007). Vortex identification: New requirements and limitations. *International journal of heat and fluid flow*, 638-652.

Koochesfahani, M. M. (1989). Vortical patterns in the wake of an oscillating airfoil. *AIAA*, 1200.

Kuethe, A. M. (1972). Effect of streamwise vortices on wake properties associated with sound generation. *Journal of Aircraft*, 715-719.

Lin, J. C. (1990). *Control of a low-speed turbulent flow over a backward-facing ramp.* Old Dominion University.

Lin, J. C. (1999). Control of turbulent boundary-layer separation using micro-vortex generators. *30th Fluid Dynamics Conference.*

Lin, J. C. (2002). Review of research on low-profile vortex generators to control boundary-layer separation. *Progress in Aerospace Sciences*, 389-420.

Lin, J. C., Howard, F. G., & Selby, G. V. (1990a). Investigation of several passive and active methods for turbulent flow separation control. *Plasma Dynamics and Lasers COnference.*

Lin, J. C., Howard, F. G., & Selby, G. V. (1990b). Small submerged vortex generators for turbulent flow separation control. *Journal of Spacecraft and Rockets*, 503-507.

Lin, J. C., Howard, F. G., & Selby, G. V. (1991). Exploratory study of vortex-generating devices for turbulent flow separation control. *29th Aerospace Sciences Meeting.*

Lissaman, P. B. (1983). Low-Reynolds-number airfoils. *Ann. Rev. Fluid Mech.*, 223-239.

Lu, P., Li, Q., & Liu, C. (2011). Numerical study of mechanism of u-shape vortex formation. *49th AIAA Aerospace Sciences Meeting.* Oriando.

Lumley, J. L. (1967). The structure of inhomogeneous turbulent flows. In A. M. Yaglom, & V. I. Tatarsky, *Atmospheric Turbulence and Radio Wave Propagation* (pp. 166-176). Moscow.

Melling, A. (1997). Tracer particles and seeding for particle image velocimetry. *Meas Sci Technol*, 1406-1416.

Pauley, W. R., & Eaton , J. K. (1994). The effect of embedded longitudal vortex arrays on turbulent boundary layer heat transfer. *Journal of Heat Transfer*, 871-879.

Pearcey, H. H. (1961). Shock induced separation and its prevention by design and boundary layer and flow control. In G. V. Lachmann, *Boundary layer and flow control, vol 2* (pp. 1166-1344). New York: Pergamon Press.

Perry, A. E., & Schofield, W. H. (1973). Mean velocity and shear stress distributions in turbulent boundary layers. *Physics Fluids*, 2068-2074.

Prasad, A. K. (2000a). Particle image velocimetry. *Current Science Bangalore*, 51-60.

Prasad, A. K. (2000b). Stereoscopic particle image velocimetry. *Exp. Fluids*, 103-116.

Prasad, A. K., & Adrian, R. J. (1993). Stereoscopic particle image velocimetry applied to liquid flows. *Exp. Fluids*, 49-60.

Raffel, M., Willert, C. E., Wereley, S. T., & Kompenhans, J. (2007). *Particle Image Velocimetry: a practical guide.* Springer.

Ramamurti, R., & Sandberg, W. (2001). Simulation of flow about flapping airfoils using finite element incompressible flow solver. *AIAA*, 253.

Rao, D., & Kariya, T. (1988). Boundary-layer submerged vortex generators for separation control - an exploratory study. *1st National Fluid Dynamics Conference.*

Scarano, F. (2013). Tomographic PIV: principles and practices. *Meas Sci Technol*, 28.

Scarano, F., & Poelma, C. (2009). Three-dimensional vorticity patterns of cylinder wakes. *Exp Fluids*, 69.

Scarano, F., David, L., Bsibsi, M., & Calluaud, D. (2005). S-PIV comparative assessment: image dewarpng + misalignment correction and pinhole + geometric back projection. *Exp. Fluids*, 257-266.

Schlichting, H., & Gersten, K. (2016). *Boundary-layer theory.* Springer.

Schubauer, G. B., & Spangenberg, W. G. (1960). Forced mixing in boundary layers. *J Fluid Mech*, 10-32.

Sears, R. L., & Telionis, D. P. (1975). Boundary-layer separation in unsteady flow. *SIAM J. Applied Math*, 215-235.

Shen, S. F. (1979). Unsteady separation according to the boundary layer equation. *Advances in Applied Mechanics*, 177-220.

Shiloh, k., Shivaprasad, B. G., & Simpson, R. L. (1981). The structure of a separating turbulent boundary layer. part III. transverse velocity measurements. *Journal of Fluid Mechanics*, 75-90.

Simpson, R. L. (1979). *Summary report on the Coloquium on flow separation.* Project SQUID Report SMU-3-PU.

Simpson, R. L. (1981). Review - a review of some phenomena in turbulent flow separation. *ASME Journal of Fluids Engineeing*, 520-533.

Simpson, R. L., Chew, Y. -T., & Schivaprasad, B. G. (1981b). The structure of a separating turbulent boundary layer. part II. Higher order turbulences results. *Journal of Fluid Mechanics*, 53-73.

Simpson, R. L., Chew, Y. -T., & Shicaprasad, B. G. (1981a). The structure of a separating turbulent boundary layer. part 1. mean flow and Reynolds stresses. *Journal of Fluid Mechanics*, 23-51.

Simpson, R. L., Strickland, J. H., & Barr, P. W. (1977). Features of a separating turbulent boundary layer in the vicinity of separation. *Journal of Fluid Mechanics*, 293-304.

Sirovich, L. (1987). Turbulence and the dynamics of coherent structures. I - Coherent structures. *Quarterly of Applied Mathematics*, 561-571.

Soloff, S. M., Adrian, R. J., & Liu, Z. C. (1997). Distortion compensation for generalized stereoscopic particle image velocimetry. *Meas Sci Technol*, 1441-1454.

Sun, Z., Schrijer, F. F., Scarano, F., & van Oudheusden, B. W. (2016). Decay of the supersonic turbulent wakes from micro-ramps. *Physics of fluids*, 025115.

Taylor, H. D. (1947). *The elimination of diffuser separation by vortex generators*. East Hartford: Uniter Aircraft Corporation.

Wendt, B. J., & Hingst, W. R. (1994). Flow structure in the wake of a wishbone vortex generator. *AIAA*, 2234-2240.

Westerweel, J., & Scarano, F. (2005). Universal outlier detection for PIV data. *Exp Fluids*, 1096-1100.

Wheeler, G. O. (1991a). *United States of America Patent No. 4455045*.

Wheeler, G. O. (1991b). *United States of America Patent No. 5058837*.

Wieneke, B. (2005). Stereo-PIV using self-calibration on particle images. *Exp Fluids*, 1096.

Wieneke, B. (2007). Volume self-calibration for stereo-PIV and tomographic-PIV. *7th Int Symp PIV*. Rome.

Wieneke, B. (2008). Volume self-calibration for 3D particle image velocimetry. *Exp Fluids*, 549-556.

Willert, C. E. (1997). Stereoscopic digital particle image velocimetry for application in wind tunnel flows. *Meas Schi Technol*, 1465-1469.

Willert, C. E., & Gharib, M. (1991). Digital particle image velocimetry. *Exp. fluids*, 181-193.

Ye, Q., Schrijer, F. F., & Scarano, F. (2016). Boundary layer transition mechanisms behind a micro-ramp. *Journal of Fluid Mechanics*, 132-161.

Zhang, J., Tao, B., & Katz, J. (1997). Turbulent flow measurement in a square duct with hybrid holographic PIV. *Exp Fluids*, 373-381.